The Astrophysical Journal, 679:762–782, 2008 May 20

MAPPING THE SHORES OF THE BROWN DWARF DESERT. I. UPPER SCORPIUS

Adam L. Kraus
Department of Astrophysics, California Institute of Technology, Pasadena, CA 91125

Michael J. Ireland
Division of Geological and Planetary Sciences, California Institute of Technology, Pasadena, CA 91125

and

Frantz Martinache and James P. Lloyd
Department of Astronomy, Cornell University, Ithaca, NY 14853
Received 2007 November 26; accepted 2008 January 14

ABSTRACT

We present the results of a survey for stellar and substellar companions to 82 young stars in the nearby OB association Upper Scorpius. This survey used nonredundant aperture mask interferometry to achieve typical contrast limits of $\Delta K \sim 5$–6 at the diffraction limit, revealing 12 new binary companions that lay below the detection limits of traditional high-resolution imaging; we also summarize a complementary snapshot imaging survey that discovered seven directly resolved companions. The overall frequency of binary companions ($\sim 35^{+5}_{-4}$ % at separations of 6–435 AU) appears to be equivalent to field stars of similar mass, but companions could be more common among lower mass stars than for the field. The companion mass function has statistically significant differences compared to several suggested mass functions for the field, and we suggest an alternate lognormal parameterization of the mass function. Our survey limits encompass the entire brown dwarf mass range, but we only detected a single companion that might be a brown dwarf; this deficit resembles the so-called brown dwarf desert that has been observed by radial velocity planet searches. Finally, our survey's deep detection limits extend into the top of the planetary mass function, reaching 8–12 $M_{\rm Jup}$ for half of our sample. We have not identified any planetary companions at high confidence ($\gtrsim$99.5%), but we have identified four candidate companions at lower confidence ($\gtrsim$97.5%) that merit additional follow-up to confirm or disprove their existence.

Subject headings: binaries: general — stars: low-mass, brown dwarfs — stars: pre–main-sequence

Online material: color figures

1. INTRODUCTION

The detection and characterization of low-mass companions have become some of the highest priorities of the astronomical community. Radial velocity (RV) surveys have discovered over 200 extrasolar planetary companions over the past decade, and both RV surveys and coronagraphic imaging surveys have discovered an abundance of stellar-mass companions (e.g., Marcy & Butler 2000; McCarthy & Zuckerman 2004; Metchev 2005[1]; Johnson et al. 2006; Naef et al. 2007). However, very few brown dwarf companions have been identified, an unexpected result given that the observational signatures of more massive companions are far larger than those of planetary-mass companions and that free-floating brown dwarfs are very common (Kirkpatrick et al. 2000; Luhman et al. 2003; Chiu et al. 2006; Slesnick et al. 2006a, 2006b). This dearth of companions between the stellar and planetary mass regimes is popularly known as the "brown dwarf desert." The existence and extent of the brown dwarf desert can provide key constraints on star and planet formation since it represents the extreme mass limit of both processes.

If the stellar-mass binary companions of solar-mass stars are drawn from the initial mass function (IMF; e.g., Kroupa 1995) or formed via some other process that preferentially forms low-mass companions (e.g., Duquennoy & Mayor 1991, hereafter DM91), then brown dwarf companions should be common unless another process inhibits their formation or dynamically strips them. However, if stellar companions are formed via the fragmentation of a protostellar core, then there are no a priori expectations that brown dwarfs should form. Indeed, even if fragmentation can form an extremely inequal-mass pair, the long collapse timescale for low-mass objects might lead to their preferential photoevaporation by the higher mass, more luminous companion.

It is also unclear whether brown dwarfs could form via planetary formation processes. RV surveys suggest that the giant planetary mass function is well fitted by a power law, $dN/dm \propto M^{-1.05}$, for masses of $\sim$1–10 $M_{\rm Jup}$ (Marcy et al. 2005). If this power law extends to higher masses, there should be as many "planetary" companions with masses of 10–25 $M_{\rm Jup}$ as with masses of 4–10 $M_{\rm Jup}$ or 1.6–4.0 $M_{\rm Jup}$. An absence of these companions suggests either that the function is not a power law or that the power law is truncated by some limit. For example, submillimeter disk surveys suggest that protoplanetary disks have a mean mass of $\sim$5 $M_{\rm Jup}$ by the age of 1–2 Myr (Andrews & Williams 2005), with a small fraction ($\sim$5%) having masses of $\sim$30–100 $M_{\rm Jup}$. Unless massive planets are formed very early or efficiently accrete the entire disk mass, this could impose an upper cutoff on the distribution of planetary masses.

The brown dwarf desert has been studied mostly at very small or very large separations. The RV exoplanet surveys that have proven so successful over the past decade should have detected any brown dwarfs within their outer separation limit ($\sim$3–5 AU), and they have set very low upper limits on the frequency of close brown dwarf companions to solar-mass stars ($<$1%; Marcy & Butler 2000; Grether & Lineweaver 2006). Similarly,

[1] See http://etd.caltech.edu/etd/available/etd-08262005-170055/.

high-resolution coronagraphic imaging surveys have demonstrated sufficient sensitivity to identify brown dwarf companions at typical separation limits of >50 AU (e.g., Gizis et al. 2001; Neuhäuser et al. 2003; McCarthy & Zuckerman 2004; Neuhäuser & Guenther 2004; Metchev 2005). They have measured frequencies that are low, but somewhat inconsistent (and perhaps not anomalously low; 1% ± 1% by McCarthy & Zuckerman [2004], compared to $6.8^{+8.3}_{-4.9}$ % by Metchev [2005] and 18% ± 14% by Gizis et al. [2001]). A survey for wide companions to high-mass (2–8 $M_{\odot}$) stars in Upper Sco by Kouwenhoven et al. (2007) found a relatively low frequency for brown dwarf companions, 0.5% ± 0.5% at separations of 130–520 AU. Finally, there have been an intriguing sample of candidate planetary-mass companions identified at large separations (e.g., Chauvin et al. 2004; Neuhäuser et al. 2005), but both their mass and formation mechanism are still uncertain and their frequency is still unconstrained (e.g., Masciadri et al. 2005; Kraus et al. 2006; Biller et al. 2007; Ahmic et al. 2007).

However, these surveys do not study the actual separation range where most giant planets and binary companions are expected to form. Most giant planets at small orbital radii ($\lesssim$5 AU) are thought to have migrated inward, so their mass distribution may not match that of their more distant brethren. The binary formation process may also be different for small separations ($\lesssim$10 AU), with H_2 dissociation softening the equation of state and leading to enhanced fragmentation over that expected for larger length scales (Whitworth & Stamatellos 2006). Similarly, giant planets are not expected to form at very large radii ($\gtrsim$30 AU) since the formation timescale is too long, and the frequency of wide binary companions may differ significantly from those of closer binaries (e.g., Kraus & Hillenbrand 2007a) since the fragmentation occurs on a length scale that is several orders of magnitude larger.

Ideally, the desert should be studied at the separation range where giant planets and most binaries are thought to form (~5–30 AU; Lissauer & Stevenson 2007; DM91), but this has been impossible using existing techniques. For example, theoretical models (Chabrier et al. 2000) suggest that a 50 $M_{\rm Jup}$ brown dwarf located 15 AU (1″–2″) from a nearby field star will have a contrast ratio of $\Delta K \sim$ 10–15 mag at a separation of only ~1″. The contrast problem could have been addressed by observing young stars since their substellar companions would be intrinsically more luminous ($\Delta K < 5$ mag), but most young stars are farther away, so the separations are even smaller (0.1″–0.2″; $\sim\lambda/D$). Sensitivities near the diffraction limit have traditionally been far too shallow to detect such companions. However, new advances in high-resolution imaging techniques are now opening up this critical regime; our survey uses one such technique, nonredundant aperture mask interferometry.

The technique of nonredundant aperture masking has been well established as a means of achieving the full diffraction limit of a single telescope (e.g., Nakajima et al. 1989; Tuthill et al. 2000). The reason for the technique's success over direct imaging is that the calibration is independent of structure of the wave front over scales larger than a single subaperture, but it still preserves the angular resolution of the full aperture. This technique, when applied to seeing-limited observations, requires observations to be taken in a speckle mode with subapertures of diameter smaller than the atmospheric coherence length, limiting the technique to objects brighter than about $m_H = 5$. The use of adaptive optics (AO) allows for longer integration times and larger subapertures, extending the technique to much fainter targets.

Published detections have been able to recover astrometrically discovered binary systems with contrast ratios of 3:1 at $0.6\lambda/D$ and 100:1 at λ/D (Pravdo et al. 2006; Lloyd et al. 2006; Ireland et al. 2008) using total observation times of ~10 minutes. The inner limit of companion detectability at high contrast is $\lambda/2B_L$, where B_L is the longest baseline in the mask (typically 80%–95% of the aperture diameter). Typical closure phase errors are such that aperture masking can unveil high-contrast companions at separations 5 times closer than direct imaging in both H and K bands.

In this paper we describe an aperture mask interferometry and direct imaging survey to detect stellar and substellar companions to young stars in the nearby OB association Upper Scorpius. This survey directly studies the age and separation range corresponding to the peak of planet formation, offering the first glimpse of the brown dwarf desert in this critical range of parameter space. In § 2 we describe our survey sample, and in § 3 we describe the observations and data analysis techniques. In § 4 we summarize the results of our survey. In § 5 we combine these results with previous binary surveys to place constraints on the stellar binary frequency, mass function, and separation distribution, and in § 6 we consider constraints on the corresponding parameters for the planetary population. Finally, in § 7 we discuss the implications of our survey for the extent and aridity of the brown dwarf desert.

2. SURVEY SAMPLE

Upper Sco is an ideal target for large-scale surveys to detect brown dwarf or planetary companions. It is young enough (~5 Myr) that substellar companions are much more luminous than those of typical field stars, and this age is thought to be the peak epoch of giant planet formation (Lissauer & Stevenson 2007 and references therein). Its relative proximity (~145 pc; de Zeeuw et al. 1999) also means that the resolution limit of large telescopes (~40–100 mas; 6–15 AU) corresponds to the giant planet separation regime of our own solar system. Finally, the association has been very intensely studied, with several hundred members identified in the past decade, so it provides a much larger sample of well-characterized members than nearby moving groups.

We compiled a preliminary list of 356 targets from the known members of Upper Sco as compiled in Kraus & Hillenbrand (2007a); this census included all spectroscopically confirmed members with spectral type G0 or later from the recent surveys by Walter et al. (1994), Preibisch et al. (1998, 2001, 2002), Kunkel (1999), Ardila et al. (2000), Martin et al. (2004), and Slesnick et al. (2006a). We also added two stars that were not included in that census: RX J1550.9−2534 (which was originally classified as F9 by the HD catalog but was reclassified as G1 by the Michigan Spectral Survey; Houk & Smith-Moore 1988) and V1149 Sco (which was not included in any large membership surveys since it was identified as a young star before they were conducted; Stephenson 1986).

All of our observations have been conducted from northern sites, so we removed 25 of the 26 stars south of $\delta = -25^{\circ}$ from further consideration. The only exception was RX J1550.9−2534, which we retained in order to make a complete group of four science targets of similar brightness and air mass. As we describe below, preliminary imaging showed that it was an obvious binary that is not suitable for masking observations anyway, but we retain it in our sample for statistical purposes. We also rejected 230 of the remaining low-mass association members that were optically fainter than the useful limit of the AO system ($R \gtrsim 14$). Finally, we removed the 23 known binaries with separations of <3″. In close systems, the stellar companion would have dominated the signal in our observations, complicating any search for fainter companions. Wider binaries (with separations near the seeing limit) were rejected because they are generally not corrected well by the AO system, although we still observed several of them with direct imaging in order to test whether this would actually occur. A total

of seven targets were not discovered to be binaries until we arrived at the telescope and obtained quick direct imaging observations; these targets were also removed from the aperture mask sample. We mistakenly removed one more target, USco 160643.8−190805, that we initially thought was a binary based on direct imaging. Subsequent analysis showed that it was flagged as a binary erroneously; we do not consider it in our statistical sample because we only have imaging data and not masking data.

These cuts left a total of 72 Upper Sco members in our aperture mask sample, plus 11 members (10 known or new binary systems and 1 erroneous omission) that we only observed with direct imaging. We list all of these targets in Table 1, where we also include each target's spectral type (adopted from the discovery survey), mass (as determined in § 3.3), and R and K magnitudes, plus the target group that it was observed with (as described in § 3.1). In Table 2 we list the 19 known binary systems that would have passed our selection criteria. We did not observe any of these systems, but we include them in our sample for determining stellar binary statistics since they have known binary companions. Our upper limits on the existence of planetary-mass companions will not include any known or newly discovered binary systems.

3. OBSERVATIONS AND DATA ANALYSIS

3.1. *Observations*

We observed our target sample in 2007 April–July with the Keck II 10 m and Palomar Hale 200″ telescopes. All observations were obtained using the facility AO imagers, NIRC2 and PHARO. Both instruments have aperture masks permanently installed at or near the pupil plane in filter or pupil stop wheels. The seeing quality was well above average for most of the Keck observations, yielding superb AO correction for bright targets and acceptable Strehl ratios (∼15%–20%) even for targets as faint as $R \sim 14$. The Palomar observations were obtained under approximately median conditions (∼1″ seeing).

All observations conducted at Keck were obtained with a K' filter, while those conducted at Palomar were obtained with a methane short filter, which is in H band (central wavelength 1.57 μm, bandpass 0.1 μm). This filter was used instead of full H band because of calibration errors related to dispersion that had been found in previous data sets. This strategy allowed us to achieve similar resolution limits at both telescopes, despite the smaller aperture size at Palomar. Our Palomar observations suffered a modest loss of sensitivity since the Strehl is lower in H than in K', but the typical sensitivity limit in H still allows us to detect a $\sim 30\ M_{\rm Jup}$ companion at 40 mas for half of our sample members. Observing in K would have yielded limits of $\Delta K \lesssim 1$ mag deeper (equivalent to $\Delta H \lesssim 1.5$ since low-mass companions are redder in $H - K$), and we decided that this was not as important since the corresponding detection limits ($\gtrsim$15–20 $M_{\rm Jup}$) could not have reached the planetary mass range.

Observations at Keck used a nine-hole mask, with the longest baseline 8.27 m and the shortest baseline 1.67 m. We used a multiple-correlated double sampling readout in a 512×512 subarray of the ALADDIN detector, with 16 endpoint reads and a 10 s exposure per frame. Observations at Palomar with PHARO also used a nine-hole mask, with the longest baseline 3.94 m and the shortest baseline 0.71 m. To maximize the number of reads, we used either a 256×256 or 150×150 subarray mode in one quadrant of the HAWAII detector, with a total of 16 or 28 reads, respectively, per array reset. Every read was saved to disk, so that in postprocessing each file could be split into subframes. Splitting the data into more subframes minimizes sensitivity to changing seeing or AO instabilities, and using less subframes minimizes sensitivity to readout noise. We found that for the typical magnitudes of our targets, signal-to-noise ratio was optimized by using read pairs separated by one read: giving 862 ms exposure times for the 256×256 subarray mode, and 430 ms exposure times for the 150×150 subarray mode.

A key requirement for obtaining good contrast limits is the contemporaneous observation of calibrator sources, ideally single stars that are nearby on the sky and similar in both optical and near-infrared (NIR) brightness. A typical observing mode for isolated field stars is to obtain several sets of observations for a science target, interspersing visits to calibrator stars between each science observation. As a result, observations for a single science target might require as many as six target acquisitions (three calibrators, plus three visits to the source). However, all of our science targets are located in close proximity on the sky ($<10^{\circ}$) and they span a continuous range of brightness, so we were able to use the same calibrator star for multiple science targets and to intercalibrate between science targets. To this end, we divided our sample into 20 groups of approximately four similar-brightness stars each and then observed each group contemporaneously. Specifically, we visited each group member three times, plus we obtained one visit for each of two independent field calibrators. This allowed us to typically observe four science targets with a total of 14 acquisitions, for an average of 3.5 acquisitions per target. The average total time per acquisition was ∼4 minutes, so our strategy required ∼15 minutes per target.

We summarize the composition of our target groups and list the independent calibrators in Table 3. We also include the observation date and the mean R and K magnitudes for each group. Some of our groups are bigger or smaller because our acquisition images showed that several intended targets were resolved binaries (§ 3.3). When this occurred, we removed the binary system from our sample; in the case of groups 12–15, we found a large number of binaries, so we rearranged the group composition at the telescope and eliminated group 13.

Finally, a large fraction of our sample has been observed previously with high-resolution imaging (Brandner et al. 1996; Metchev 2005; Bouy et al. 2006), so we knew a priori whether these stars had known companions. However, many of our targets have been observed only with speckle imaging (Köhler et al. 2000) or have not been observed with any high-resolution techniques. For these sources, we decided to obtain quick observations in direct imaging mode in order to screen out obvious binaries. This also allowed us to test for companions at separations outside the nominal limit of aperture mask interferometry (240 mas at Palomar and 320 mas at Keck).

In Table 4 we list all of the sources that were observed with direct imaging and summarize the observations. We observed all of these sources with NIRC2 or PHARO using the smallest pixel scale available (10 or 25 mas pixel^{-1}, respectively) and a two-point diagonal dither pattern. Faint stars were observed with a K' or K_s filter, while bright stars that would have saturated the detector were observed with a Brγ filter, which attenuates flux by a factor of ∼10 relative to broadband K filters.

3.2. *Aperture Mask Analysis and Detection Limits*

The aperture masking analysis pipeline is similar to that used for several previous papers containing Palomar masking data (Pravdo et al. 2006; Lloyd et al. 2006; Martinache et al. 2007). After subtracting the bias (dark) level, flat-fielding, and removing bad pixels, the data are windowed by a super-Gaussian [a function of the form $\exp(-kx^4)$]. This window both limits sensitivity to readout noise and acts as a spatial filter. Each frame is then Fourier-transformed and the complex visibility extracted for each baseline.

TABLE 1
UPPER SCO SAMPLE

Name	R.A. (J2000.0)	Decl. (J2000.0)	Spectral Type	Mass ($M_\odot$)	R (mag)	K (mag)	Group
RX J1550.0−2312	15 50 04.99	−23 11 53.7	M2	0.49	13.1	8.93	14
RX J1550.9−2534	15 50 56.42	−25 34 19.0	G1	1.75	9.4	7.91	...
RX J1551.1−2402	15 51 06.61	−24 02 19.0	M2	0.49	13.5	9.73	17
RX J1557.8−2305	15 57 50.03	−23 05 09.4	M0	0.68	12.7	9.27	12
RX J1558.1−2405	15 58 08.15	−24 05 53.0	K4	0.95	11.4	8.96	8
RX J1558.2−2328	15 58 12.71	−23 28 36.4	G2	1.66	9.9	8.02	1
RX J1600.2−2417	16 00 13.30	−24 18 10.6	M0	0.68	13.1	9.51	14
RX J1600.6−2159	16 00 40.57	−22 00 32.2	G9	1.43	10.2	8.44	3
RX J1600.7−2127	16 00 42.77	−21 27 38.0	K7	0.77	11.7	8.92	10
RX J1601.1−2113	16 01 08.01	−21 13 18.5	M0	0.68	12.0	8.80	9
RX J1601.9−2008	16 01 58.23	−20 08 12.2	G5	1.62	9.9	7.67	2
RX J1602.0−2221	16 02 00.39	−22 21 23.7	M1	0.60	12.8	8.84	12
RX J1602.8−2401B	16 02 51.24	−24 01 57.4	K4	0.95	11.1	8.93	4
RX J1602.8−2401A	16 02 52.43	−24 02 22.7	K0	1.35	10.4	7.65	1
RX J1603.6−2245	16 03 35.50	−22 45 56.1	G9	1.43	10.6	8.36	3
RX J1603.9−2031A	16 03 57.68	−20 31 05.5	K5	0.87	12.0	8.37	10
RX J1604.3−2130	16 04 21.66	−21 30 28.4	K2	1.12	11.8	8.51	11
RX J1605.6−2152	16 05 39.36	−21 52 33.8	M1	0.60	13.6	9.47	17
RX J1606.2−2036	16 06 12.54	−20 36 47.3	K5	0.87	12.5	8.90	12
RX J1607.0−2043	16 07 03.73	−20 43 07.4	M1	0.60	13.6	9.53	17
RX J1607.0−2036	16 07 03.56	−20 36 26.5	M0	0.68	11.3	8.10	...
USco 155655.5−225839	15 56 55.46	−22 58 40.4	M0	0.68	13.2	9.43	14, 15
USco 160142.6−222923	16 01 42.55	−22 29 23.9	M0	0.68	13.8	10.22	19
USco 160341.8−200557	16 03 41.87	−20 05 57.8	M2	0.49	13.7	9.49	18
USco 160343.3−201531	16 03 43.35	−20 15 31.5	M2	0.49	13.7	9.72	18
USco 160428.4−190441	16 04 28.39	−19 04 41.4	M3	0.36	13.6	9.28	...
USco 160517.9−202420	16 05 17.92	−20 24 19.5	M3	0.36	13.3	9.14	15
USco 160643.8−190805	16 06 43.86	−19 08 05.6	K6	0.82	12.8	9.20	...
USco 160707.7−192715	16 07 07.67	−19 27 16.1	M2	0.49	13.8	9.80	19
USco 160801.4−202741	16 08 01.42	−20 27 41.7	K8	0.68	13.0	9.29	16
USco 160822.4−193004	16 08 22.34	−19 30 05.2	M1	0.60	12.9	9.06	12
USco 160823.2−193001	16 08 23.25	−19 30 00.9	K9	0.68	13.2	9.47	15
USco 160823.8−193551	16 08 23.88	−19 35 51.8	M1	0.60	13.3	9.25	...
USco 160825.1−201224	16 08 25.11	−20 12 24.6	M1	0.60	13.9	9.87	20
USco 160900.7−190852	16 09 00.76	−19 08 52.6	K9	0.68	13.1	9.15	15
USco 160908.4−200928	16 09 08.45	−20 09 27.8	M4	0.24	13.8	9.52	...
USco 160916.8−183522	16 09 16.85	−18 35 22.6	M2	0.49	14.0	9.67	20
USco 160946.4−193735	16 09 46.44	−19 37 36.1	M1	0.60	13.8	9.63	19
USco 160954.4−190654	16 09 54.41	−19 06 55.1	M1	0.60	13.7	9.60	18
USco 161031.9−191305	16 10 31.96	−19 13 06.2	K7	0.77	13.0	8.99	12
USco 161115.3−175721	16 11 15.34	−17 57 21.4	M1	0.6	13.2	9.20	15
USco 161347.5−183459	16 13 47.51	−18 35 00.4	M2	0.49	14.1	9.91	20
USco 161358.1−184828	16 13 58.15	−18 48 29.0	M2	0.49	14.0	9.88	20
GSC 06764−01305	15 35 57.80	−23 24 04.6	K3	0.99	12.0	9.43	11
GSC 06195−00768	15 57 02.34	−19 50 42.0	K7	0.77	11.1	8.37	...
GSC 06191−00019	15 59 02.09	−18 44 14.3	K6	0.82	11.1	8.11	...
GSC 06191−00552	15 58 47.70	−17 57 59.0	K3	0.99	11.5	8.33	5
GSC 06204−00812	16 03 02.69	−18 06 05.0	K4	0.95	11.3	8.73	5
GSC 06204−01067	16 03 23.68	−17 51 42.3	M2	0.49	12.4	8.61	...
GSC 06208−00834	16 06 31.70	−20 36 23.3	K6	0.82	12.4	8.73	10
GSC 06209−00735	16 08 14.74	−19 08 32.8	K2	1.12	11.0	8.43	5
GSC 06205−00954	16 08 31.38	−18 02 41.4	M0	0.68	12.2	8.91	9
GSC 06209−01501	16 08 56.73	−20 33 46.0	K5	0.87	11.9	8.62	9
GSC 06213−01358	16 09 30.30	−21 04 58.9	M0	0.68	12.1	8.92	9
GSC 06213−00194	16 09 40.99	−22 17 59.4	M0	0.68	11.6	8.44	7
GSC 06213−00306	16 10 42.03	−21 01 32.0	K5	0.87	11.9	8.56	6
GSC 06793−00868	16 11 56.33	−23 04 05.1	M1	0.6	12.2	8.82	...
GSC 06793−00797	16 13 02.72	−22 57 44.6	K4	0.95	11.7	8.46	8
GSC 06213−00306	16 13 18.59	−22 12 48.9	G9	1.43	9.8	7.43	1, 2
GSC 06793−00994	16 14 02.12	−23 01 02.2	G4	1.63	10.9	8.61	4
GSC 06793−00806	16 15 34.57	−22 42 42.1	M1	0.60	11.2	7.91	7
GSC 06793−01406	16 16 17.95	−23 39 47.7	G7	1.56	9.9	8.10	2
GSC 06214−02384	16 19 33.96	−22 28 29.4	K0	1.35	10.5	8.51	3
GSC 06794−00480	16 20 45.96	−23 48 20.9	K3	0.99	11.9	8.93	8
GSC 06214−00210	16 21 54.67	−20 43 09.1	M1	0.60	11.6	9.15	8

TABLE 1—*Continued*

Name	R.A. (J2000.0)	Decl. (J2000.0)	Spectral Type	Mass ($M_\odot$)	R (mag)	K (mag)	Group
GSC 06794−00537	16 23 07.83	−23 00 59.7	K2	1.12	11.0	8.18	4
GSC 06794−00156	16 24 51.36	−22 39 32.5	G6	1.59	9.3	7.08	1
GSC 06794−00337	16 27 39.56	−22 45 23.0	K1	1.25	10.9	8.08	6
GSC 06228−01359	16 35 48.36	−21 48 39.7	M0	0.68	12.4	8.48	10
ScoPMS 015	15 57 19.99	−23 38 50.0	M0	0.68	12.4	8.88	...
ScoPMS 017	15 57 34.31	−23 21 12.3	M1	0.60	12.9	8.99	14
ScoPMS 019	15 59 59.95	−22 20 36.8	M1	0.60	12.3	8.63	11
ScoPMS 021	16 01 25.64	−22 40 40.3	K1	1.25	13.6	8.52	16
ScoPMS 022	16 02 08.45	−22 54 58.9	M1	0.60	13.4	9.55	17
ScoPMS 027	16 04 47.76	−19 30 23.1	K2	1.12	11.0	8.04	5
ScoPMS 028	16 05 27.27	−19 38 46.6	M1	0.60	13.3	9.55	16
ScoPMS 042b	16 10 21.74	−19 04 06.7	M3	0.36	13.8	9.62	19
ScoPMS 044	16 11 08.91	−19 04 46.9	K2	1.12	11.3	7.69	7
ScoPMS 045	16 11 20.58	−18 20 54.9	K5	0.87	11.4	8.56	6
ScoPMS 048	16 11 59.28	−19 06 53.3	K0	1.35	11.1	8.09	7
ScoPMS 060	16 17 31.39	−23 03 36.0	G0	1.71	9.7	7.97	2
ScoPMS 214	16 29 48.70	−21 52 11.9	K0	1.35	10.5	7.76	4
V1149 Sco	15 58 36.90	−22 57 15.0	G7	1.56	10.2	7.05	3

NOTES.—Units of right ascension are hours, minutes, and seconds, and units of declination are degrees, arcminutes, and arcseconds. Typical uncertainties are ∼1 subclass for spectral types, ∼0.2 mag for R magnitudes (taken from NOMAD; Zacharias et al. 2004), and ∼0.02 mag for K magnitudes (taken from 2MASS; Skrutskie et al. 2006). The uncertainties in mass are dominated by systematic errors, including a global zero-point uncertainty of ∼20% and individual uncertainties of as much as ∼100% due to the possibility of further unresolved multiplicity.

Complex visibilities cannot be directly used for high-fidelity measurements because of their sensitivity to variable optical aberrations and noncommon path errors. Instead, we use the averaged squared visibility and the complex triple product (Lohmann et al. 1983). For each visit to each star, we extract squared visibility, closure phase, and the uncertainties on these quantities based on the scatter within one visit. Finally, the calibration process consists of estimating the instrumental squared visibilities and closure phases. The target star's squared visibilities are divided by the instrumental squared visibilities, and the instrumental closure phase is subtracted from the measured closure phase.

Figures 1 and 2 show a fit to data for the 27 mas separation binary RX J1550.0−2312. Squared visibility is plotted against baseline projected along the axis of the binary. As closure phase is a multidimensional quantity, we chose to simply plot the measured closure phases versus the model closure phases. Despite this binary being at a separation of only $0.6\lambda/D$, it is clear that it is an extremely high signal-to-noise ratio detection. Note that

TABLE 2
KNOWN BINARY SYSTEMS

Primary	R.A. (J2000.0)	Decl. (J2000.0)	Primary Spectral Type	$M_{\rm prim}$ ($M_\odot$)	R (mag)	K (mag)	ΔK (mag)	Separation (mas)	P.A. (deg)	References
GSC 06780−01061	16 06 54.36	−24 16 10.8	M3	0.36	12.2	8.86	1.3	1500	270.0	1
GSC 06793−00569	16 13 29.29	−23 11 07.5	K1	1.25	11.1	8.49	2.7	1430	91.4	2
GSC 06793−00819	16 14 11.08	−23 05 36.2	K0	1.35	10.0	7.46	0.21	222	304.8	2
RX J1600.5−2027	16 00 31.35	−20 27 05.0	M1	0.60	12.8	8.83	0.43	189	171.7	3
RX J1601.7−2049	16 01 47.43	−20 49 45.8	M0	0.68	12.4	8.61	0.58	205	324.7	3
RX J1601.8−2445	16 01 51.49	−24 45 24.9	K7	0.77	11.4	8.49	1.00	76	289.6	3
RX J1602.9−2022	16 02 53.96	−20 22 48.1	K7	0.77	11.7	8.19	0.18	310	5.3	3
RX J1603.9−2031B	16 03 54.96	−20 31 38.4	M0	0.68	12.5	8.62	0.53	121	140.9	3
RX J1606.6−2108	16 06 37.41	−21 08 40.5	M1	0.60	13.2	9.11	0.09	1279	33.9	3
RX J1607.0−1911	16 07 03.94	−19 11 33.9	M1	0.60	13.4	9.22	1.47	599	87.6	3
ScoPMS 005	15 54 59.86	−23 47 18.2	G2	1.66	8.6	7.03	1.99	766	232.0	3
ScoPMS 013	15 56 29.42	−23 48 19.8	M1.5	0.54	11.6	8.75	0.62	92	169.8	3
ScoPMS 016	15 57 25.76	−23 54 22.0	M0.5	0.64	13.1	9.09	0.63	1324	226.0	3
ScoPMS 020	16 01 05.19	−22 27 31.2	M3	0.36	12.9	8.75	0.60	193	313.7	3
ScoPMS 023	16 02 10.45	−22 41 28.0	K5	0.87	10.2	8.06	0.65	300	345.6	3
ScoPMS 029	16 05 42.67	−20 04 15.0	M2	0.49	13.4	9.16	0.56	643	352.6	3
ScoPMS 031	16 06 21.96	−19 28 44.6	M0.5	0.64	12.8	8.62	0.64	578	148.2	3
ScoPMS 042a	16 10 28.58	−19 04 47.0	M1	0.60	13.0	8.71	0.42	299	84.1	3
ScoPMS 052	16 12 40.51	−18 59 28.3	K0	1.35	10.4	7.49	1.10	144	162.2	2

NOTES.—Units of right ascension are hours, minutes, and seconds, and units of declination are degrees, arcminutes, and arcseconds. Typical uncertainties are ∼1 subclass for spectral types, ∼0.2 mag for R magnitudes (taken from NOMAD; Zacharias et al. 2004), and ∼0.02 mag for K magnitudes (taken from 2MASS; Skrutskie et al. 2006). The uncertainties in masses are dominated by systematic errors, including a global zero-point uncertainty of ∼20% and individual uncertainties of as much as ∼100% due to the possibility of further unresolved multiplicity. Typical uncertainties in binary properties are ∼0.1 mag in ΔK, ∼10 mas in separation, and ∼1° in P.A.

REFERENCES.—(1) Kraus & Hillenbrand 2007a; (2) Metchev 2005; (3) Köhler et al. 2000.

TABLE 3

APERTURE MASK OBSERVATIONS

Group	Science Targets	Calibrator Stars	Telescope	R (mag)	K (mag)	Epoch (JD −2,450,000)
1.....	GSC 06213−00306, GSC 06794−00156, RX J1558.2−2328, RX J1602.8−2401A	2M 1618−2245, 2M 1613−2218	Keck	9.3–10.4	7.08–8.02	4257
2.....	GSC 06213−00306, GSC 06793−01406, RX J1601.9−2008, ScoPMS 060	2M 1602−1945, 2M 1617−2320	Palomar	9.7–9.9	7.43–8.10	4251
3.....	GSC 06214−02384, RX J1600.6−2159, RX J1603.6−2245, V1149 Sco	2M 1559−2303, 2M 1620−2231	Palomar	10.2–10.6	7.05–8.36	4252
4.....	GSC 06793−00994, GSC 06794−00537, RX J1602.8−2401B, ScoPMS 214	2M 1613−2311, 2M 1630−2118	Palomar	10.5–11.1	7.76–8.93	4312
5.....	GSC 061901−00552, GSC 06204−00812, GSC 06209−00735, ScoPMS 027	2M 1558−1747, 2M 1606−1924	Palomar	11.0–11.5	8.04–8.73	4250
6.....	GSC 06213−00306, GSC 06794−00337, ScoPMS 045	2M 1610−1818, 2M 1629−2245	Palomar	10.9–11.9	8.08–8.56	4251
7.....	GSC 06213−00194, GSC 06793−00806, ScoPMS 044, ScoPMS 048A	2M 1609−2216, 2M 1611−1906	Palomar	11.1–11.6	7.69–8.44	4252
8.....	GSC 06793−00797, GSC 06794−00480, GSC 06214−00210, RX J1558.1−2405	2M 1622−2036, 2M 1558−2412	Palomar	11.4–11.9	8.46–9.15	4252
9.....	GSC 06205−00954, GSC 06209−01501, GSC 06213−01358, RX J1601.1−2113	2M 1601−2123, 2M 1608−2022	Palomar	11.9–12.2	8.62–8.92	4250
10.....	GSC 06208−00834, GSC 06228−01359, RX J1600.7−2127, RX J1603.9−2031A	2M 1602−2133, 2M 1635−2204	Palomar	11.7–12.4	8.37–8.92	4250
11.....	GSC 06764−01305, GSC 06793−00868, RX J1604.3−2130, ScoPMS 019	2M 1613−2303, 2M 1535−2330	Keck	11.8–12.3	8.51–9.43	4257
12.....	RX J1557.8−2305, RX J1602.0−2221, RX J1606.2−2036, USco 160822.4−193004, USco 161031.9−191305	2M 1608−1916	Keck	12.4–13.0	8.61–9.27	4257
14.....	RX J1550.0−2312, RX J1600.2−2417, ScoPMS 017, USco 155655.5−225839	2M 1600−2421, 2M 1543−1929	Keck	12.8–13.0	8.99–9.29	4256
15.....	USco 155655.5−225839, USco 160517.9−202420, USco 160823.2−193001, USco 160900.7−190852, USco 161115.3−175721	2M 1557−2251, 2M 1611−1802	Keck	13.1–13.3	9.14–9.47	4257
16.....	ScoPMS 021, ScoPMS 028, USco 160801.4−202741, USco 160823.8−193551	2M 1606−1949, 2M 1607−2027, 2M 1601−2227	Keck	13.3–13.6	8.52–9.55	4257
17.....	RX J1551.1−2402, RX J1605.6−2152, RX J1607.0−2043, ScoPMS 022	2M 1550−2412, 2M 1607−2050	Keck	13.4–13.6	9.47–9.73	4256
18.....	USco 160341.8−200557, USco 160343.3−201531, USco 160908.4−200928, USco 160954.4−190654	2M 1610−1904, 2M 1614−1846	Keck	13.7–13.8	9.49–9.72	4256
19.....	ScoPMS 042b, USco 160142.6−222923, USco 160707.7−192715, USco 160946.4−193735	2M 1602−2229, 2M 1607−1929	Keck	13.8–13.8	9.62–10.22	4256
20.....	USco 160825.1−201224, USco 160916.8−183522, USco 161347.5−183459, USco 161358.1−184828	2M 1614−1846, 2M 1608−2008	Keck	13.9–14.1	9.67–9.91	4256

TABLE 4
Direct Imaging Observations

Name	Telescope	T_{int} (s)	Filter	Epoch (JD −2,450,000)
GSC 06191−00019	Pal	56.64	K_s	4251
GSC 06195−00768	Pal	18.41	K_s	4199
GSC 06204−01067	Pal	56.64	K_s	4252
GSC 06205−00954	Pal	56.64	K_s	4250
GSC 06208−00834	Pal	56.64	K_s	4250
GSC 06209−01501	Pal	56.64	K_s	4250
GSC 06213−00194	Pal	56.64	K_s	4251
GSC 06213−00306	Pal	56.64	K_s	4251
GSC 06213−01358	Pal	56.64	K_s	4250
GSC 06214−00210	Pal	56.64	K_s	4251
GSC 06214−02384	Pal	56.64	K_s	4251
GSC 06764−01305	Pal	56.64	K_s	4252
GSC 06793−00797	Pal	56.64	K_s	4251
GSC 06793−00806	Pal	56.64	K_s	4251
GSC 06793−00868	Pal	56.64	K_s	4252
GSC 06793−00994	Pal	56.64	K_s	4251
GSC 06794−00156	Pal	56.64	K_s	4251
GSC 06794−00480	Pal	56.64	K_s	4251
GSC 06794−00537	Pal	56.64	K_s	4251
RX J1550.0−2312	Keck	32	Brγ	4256
RX J1550.0−2312	Keck	32	Brγ	4257
RX J1550.9−2534	Keck	32	Brγ	4257
RX J1551.1−2402	Keck	32	Brγ	4256
RX J1557.8−2305	Keck	32	Brγ	4257
RX J1558.1−2405	Pal	56.64	K_s	4252
RX J1558.2−2328	Pal	56.64	K_s	4251
RX J1600.7−2127	Pal	56.64	K_s	4250
RX J1601.1−2113	Pal	56.64	K_s	4250
RX J1601.9−2008	Pal	56.64	K_s	4251
RX J1602.0−2221	Keck	32	Brγ	4257
RX J1602.8−2401A	Keck	16	Brγ	4257
RX J1602.8−2401B	Pal	56.64	K_s	4251
RX J1603.6−2245	Pal	56.64	K_s	4251
RX J1603.9−2031A	Pal	56.64	K_s	4250
RX J1604.3−2130	Pal	56.64	K_s	4252
RX J1606.2−2036	Pal	56.64	K_s	4252
RX J1607.0−2036	Pal	56.64	K_s	4251
ScoPMS 015	Pal	56.64	K_s	4250
ScoPMS 017	Keck	32	Brγ	4256
ScoPMS 019	Pal	56.64	K_s	4252
ScoPMS 022	Keck	32	Brγ	4256
ScoPMS 027	Pal	28.32	K_s	4250
ScoPMS 028	Keck	32	Brγ	4257
ScoPMS 042b	Keck	44	Brγ	4256
ScoPMS 044	Pal	56.64	K_s	4251
ScoPMS 045	Pal	56.64	K_s	4251
ScoPMS 048	Pal	56.64	K_s	4251
USco 160341.8−200557	Keck	32	Brγ	4256
USco 160428.4−190441	Keck	32	Brγ	4257
USco 160517.9−202420	Keck	32	Brγ	4257
USco 160643.8−190805	Pal	56.64	K_s	4252
USco 160707.7−192715	Keck	36	Brγ	4256
USco 160801.4−202741	Pal	56.64	K_s	4252
USco 160823.2−193001	Keck	32	Brγ	4257
USco 160823.8−193551	Keck	32	Brγ	4257
USco 160825.1−201224	Keck	32	Brγ	4256
USco 160900.7−190852	Pal	56.64	K_s	4252
USco 160908.4−200928	Keck	32	Brγ	4256
USco 160916.8−183522	Keck	32	Brγ	4256
USco 160954.4−190654	Keck	32	Brγ	4256
USco 161031.9−191305	Pal	56.64	K_s	4252
USco 161115.3−175721	Keck	32	Brγ	4257
USco 161347.5−183459	Keck	32	Brγ	4256

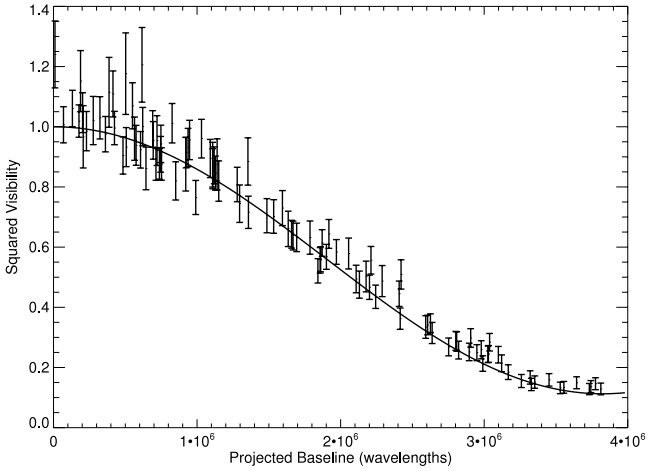

Fig. 1.—Squared visibilities as a function of projected baseline for the 27 mas binary RX J1550.0−2312. Despite a separation of only $0.6\lambda/D$, the binary system is clearly detected; the solid line denotes our best-fit value for the system parameters (Table 5).

only closure phase was used in the fit: calibration errors are evident in the squared visibility data with the few points that have squared visibility greater than 1.0.

The error analysis procedure used to calculate the covariance matrix of closure phase for each target is given in detail in the Appendix. For all targets, an attempt at fitting a binary solution was made, first by searching exhaustively in a grid in position angle and separation at high contrast and then by a gradient descent search to find the χ^2 minimum. Errors in binary parameters were calculated from the curvature of the χ^2 surface at the χ^2 minimum (i.e., the same method as most least-squares algorithms). Detections were retained if their contrast was greater than a 99.9% confidence threshold.

In order to calculate a detection threshold, we simulated 10,000 data sets with the identical (u, v)-sampling and error properties of each target. For each of these simulated data sets, we calculated the best-fit contrast ratio for every value of separation and position angle in a large grid and then tabulated the maximum contrast ratio (i.e., brightest fitted companion) within a series of annuli. Our 99.9% upper limits to companion brightness within each annulus

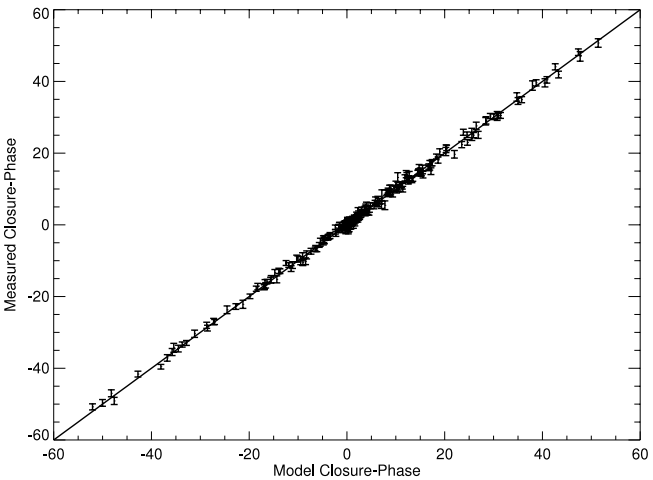

Fig. 2.—Measured closure phases as a function of modeled closure phases for RX J1550.0−2312, assuming that it has the best-fit parameters that we list in Table 5 (a 27 mas binary with a flux ratio of 2:1).

were taken to be the contrast ratio where 99.9% of the simulations had no fitted companion brighter than this limit anywhere within the annulus. Details of the simulation and fitting algorithms can be found in the Appendix.

3.3. *Imaging Analysis and Detection Limits*

The imaging data were flat-fielded and dark- and bias-subtracted using standard IRAF procedures. We measured point-spread function (PSF) fitting photometry and astrometry for our sources using the IRAF package DAOPHOT (Stetson 1987), and specifically with the ALLSTAR routine. Where possible, we analyzed each frame separately in order to estimate the uncertainty in individual measurements and to allow for the potential rejection of frames with inferior AO correction; our final results represent the mean value for all observations in a filter. If the companion could not be easily distinguished in a single filter, we measured photometry from the co-added sum of all images at each dither position.

In all cases, we used the science target (or the primary star of a binary) to produce an analytic PSF composed of a Gaussian core with Lorentzian wings. If the science target was a close binary, we reconstructed the PSF using the algorithm described in Kraus & Hillenbrand (2007b), which iteratively fits a template PSF to the primary and then subtracts the secondary to fit an improved estimate of the primary. Three sources appeared to be marginally detected in our observations; we retained these sources in our aperture mask sample and later confirmed their multiplicity (§ 4), so we processed their images with our PSF reconstruction routine and report the results. Finally, we calibrated our photometry using the known 2MASS K_s magnitudes for each of our science targets; these absolute magnitudes are uncertain by $\sim$0.1–0.2 mag due to the intrinsic variability of young stars (resulting from accretion or rotation).

At small separations ($\lesssim 5\lambda/D$), our imaging data for apparently single stars will be superseded by our aperture mask data, so the detection limits are not important. At larger separations ($\gtrsim 5\lambda/D$), where spurious sources corresponding to AO speckles dominate, we adopted the detection limits suggested by Metchev (2005) for similar observations: $\Delta K = 4$ at 250–500 mas, $\Delta K = 5$ at 500–1000 mas, and the sky background limit ($K \sim 16.5$–17.5) at separations of $\gtrsim 1''$. We tested these limits for a set of the apparently single stars in our sample by subtracting an analytic PSF from the science target, then compiling the statistics for all apparently spurious detections. In all cases, the AO speckles fall at least a magnitude below our adopted limits.

Finally, the NIRC2 images were distortion-corrected using new high-order distortion solutions (Cameron 2008) that deliver a significant performance increase as compared to the solutions presented in the NIRC2 preship manual;[2] the typical absolute residuals for bright, well-resolved stars are $\lesssim$1 mas in narrow camera mode. The PHARO images were distortion-corrected using the solution derived by Metchev (2005), with fractional uncertainties in relative astrometry of $\sim$0.15%. These uncertainties limit our astrometry for most close, well-resolved binary systems. The uncertainty for wider ($\gtrsim 2''$–$3''$) pairs seems to be driven by variation due to differential tilt jitter, while the uncertainty for close blended pairs is driven by our ability to accurately model the single-star PSF.

3.4. *Stellar and Companion Properties*

Stellar properties can be difficult to estimate, particularly for young stars, since pre–main-sequence stellar evolutionary models are not well calibrated. The mass of a given sample could be systematically uncertain by as much as 20% (e.g., Hillenbrand & White 2004), and individual masses could be uncertain by factors of 2 or more due to unresolved multiplicity or the intrinsic variability that young stars often display (from accretion or rotational modulation of star spots). This suggests that any prescription for determining stellar properties should be treated with caution.

We estimated the properties of all of our sample members using the methods described in Kraus & Hillenbrand (2007a). This procedure combines the 5 Myr isochrone of Baraffe et al. (1998) and the temperature scales of Schmidt-Kaler (1982) and Luhman et al. (2003) to directly convert observed spectral types to masses. Relative properties (mass ratios q) for all binaries in our sample were calculated by combining these isochrones and temperature scales with the empirical NIR colors of Bessell & Brett (1988) and the K-band bolometric corrections of Leggett et al. (1998) to estimate q from the observed flux ratio ΔK. We also used these techniques to estimate masses for all of our sample members, which we list in Tables 1 and 2.

For all binary systems, we have adopted the previously measured (unresolved) spectral type for the brightest component and inferred its properties from that spectral type. This should be a robust assumption since equal-flux binary components will have similar spectral types and significantly fainter components would not have contributed significant flux to the original discovery spectrum. Projected spatial separations are calculated assuming the mean distance of Upper Sco, 145 $\pm$ 2 pc (de Zeeuw et al. (1999). If the total radial depth of Upper Sco is equal to its angular extent ($\pm 8^\circ$ or $\pm$20 pc), then the unknown depth of each system within Upper Sco implies an uncertainty in the projected spatial separation of $\pm$14%. The systematic uncertainty due to the uncertainty in the mean distance of Upper Sco is negligible in comparison ($\lesssim$2%).

Finally, the sensitivity limits for some of our sample members extend to the bottom of the brown dwarf mass range and could potentially encompass the top of the planetary mass range. However, mass estimates for young giant planets are completely uncalibrated and there are ongoing debates regarding their peak and typical luminosities. The models of Baraffe et al. (2003) imply that a survey sensitive to $K \sim 16$ could detect 7–10 $M_{\rm Jup}$ planets at the distance and age of Upper Sco. However, more detailed models of planet formation by Marley et al. (2007) suggest that the typical luminosity of a young planet could be 1–2 orders of magnitude lower than previously predicted. These models differ primarily in their treatment of the initial conditions; recent models suggest that accretion shocks could dispel much of the initial energy, leading to lower internal entropy and correspondingly lower initial temperatures than the earlier models predicted. We cannot currently resolve this controversy, so we only note that our limits on the presence of massive planets should be considered with caution.

4. NEW COMPANIONS IN UPPER SCO

Our aperture mask survey is sensitive to companions with separations between $\sim\lambda/4D$ and $\sim 6\lambda/D$ (at Keck) or $\sim 4\lambda/D$ (at Palomar), corresponding to separation ranges of $\sim$10–320 mas and $\sim$20–240 mas, respectively. In this separation range, we identified 12 members of Upper Sco that possess a candidate companion at a confidence level of $\gtrsim$99.5% (99.9% per annulus); the other 60 masking sample members appear to be single to within the detection limits we derived in § 3.2. In Table 5 we list all of our newly identified candidate companions and report their flux ratios, separations, and position angles. In Table 6 we summarize our derived upper limits as a function of separation for the 60 remaining

[2] See http://www2.keck.hawaii.edu/realpublic/inst/nirc2/.

TABLE 5
Companions Identified with the Aperture Mask

Primary	Telescope	Δm (mag)	Separation (mas)	P.A. (deg)
GSC 06209−00735[a]	Palomar	2.44 ± 1.16	24.6 ± 5.2	42.5 ± 3.6
GSC 06764−01305	Keck	2.97 ± 0.01	54.68 ± 0.16	173.76 ± 0.19
GSC 06794−00156	Keck	0.45 ± 0.01	44.30 ± 0.07	230.74 ± 0.08
RX J1550.0−2312	Keck	0.76 ± 0.01	26.95 ± 0.05	222.13 ± 0.13
RX J1550.0−2312	Keck	0.76 ± 0.01	26.93 ± 0.04	222.07 ± 0.11
RX J1558.1−2405	Palomar	2.48 ± 0.09	227.67 ± 1.99	99.23 ± 0.47
RX J1601.9−2008	Palomar	2.14 ± 0.13	39.31 ± 1.57	217.67 ± 0.59
ScoPMS 017	Keck	0.78 ± 0.01	53.86 ± 0.19	68.93 ± 0.20
ScoPMS 019	Keck	0.03 ± 0.01	25.40 ± 0.12	113.55 ± 0.62
ScoPMS 027	Palomar	0.70 ± 0.03	43.18 ± 0.12	68.63 ± 0.29
USco 160517.9−202420	Keck	0.40 ± 0.07	16.15 ± 0.59	251.12 ± 1.11
USco 160707.7−192715	Keck	2.33 ± 0.01	105.25 ± 0.21	0.90 ± 0.09
USco 161031.9−191305	Keck	2.96 ± 0.02	145.55 ± 0.43	81.63 ± 0.14
Calibrators				
2M 1535−2330	Keck	1.35 ± 0.01	92.35 ± 0.17	311.46 ± 0.09
2M 1601−2227	Keck	0.64 ± 0.09	249.76 ± 0.5	328.73 ± 0.14
2M 1613−2218	Keck	3.97 ± 0.07	93.33 ± 1.04	11.9 ± 0.6

[a] The contrast ratio and separation are highly degenerate at separations this small, but at the least favorable separation, the secondary flux still represents a >7 σ detection.

members of our sample. The detection limits decline rapidly between $\sim\lambda/4D$ and $\sim 2\lambda/3D$, but they are relatively flat at larger separations, extending to contrast ratios of ∼5.0–6.5 mag at Keck and ∼4.5–5.5 mag at Palomar.

The system RX J1550.0−2312 was observed on separate nights with separate calibrator sets at Keck in order to confirm the accuracy and repeatability of our measurements. The separations and contrast ratios measured at each epoch agree to within $<1\ \sigma$, suggesting that our results are repeatable and our assessed uncertainties are valid. We also note that three of our calibrators appear to have companions. We did not use these observations in our final data calibration, and we report their astrometry in Table 4 for completeness. Finally, we note that the system GSC 06209−00735 has been previously identified as an SB1 by Guenther et al. (2007). The orbital period that they derived (2045 ± 16 days) is consistent with the projected separation (25 ± 5 mas; 3.6 ± 0.7 AU) of our newly imaged companion, so these detections appear to denote the same companion. Two more astrometric detections should allow us to resolve the orbital parameters that were not determined in the RV orbit ($K2$, i, and Ω) and directly measure the masses of both stars.

In Table 7 we summarize the observed properties of seven newly detected binary systems discovered in our snapshot imaging program, three systems that were discovered in our aperture mask survey and subsequently recovered in our imaging data, and nine known binary systems for which we report updated properties. In Figure 3 we show the corresponding discovery images for our newly discovered binaries. We do not report any new candidate companions discovered outside a radius of 2″ or with $K \geq 15$ because of the significant probability that any such companions are background stars. We have previously estimated the density of background stars brighter than $K \sim 15$ to be ∼1 arcmin^{-2} (Kraus & Hillenbrand 2007a), so the expected number of such contaminants inside ∼3″ is only ∼1. However, there are many background bulge giants with apparent brightness $K \sim 16$–17 that could be mistaken for faint wide companions, so an extension of these limits will require second-epoch observations to confirm common proper motion. Finally, we note that four of these sources fell near or inside the detection limits of the speckle interferometry survey of Köhler et al. (2000); their nondetection is most likely explained by an unfavorable orbital phase in 1994–1995 and 14 years of orbital motion.

In Table 8 we list the inferred stellar and binary properties for each of our newly identified binary systems and the binary systems that we collated from the literature. In Figures 4 and 5 we plot the contrast ratio and mass ratio versus the separation of all of our newly detected companions, plus the corresponding detection limits for apparently single stars. The vast majority of our newly identified candidate companions sit well above our survey's detection limits, suggesting that they are all valid detections. Their typical flux ratios ($\Delta K \lesssim 3$) indicate that they have stellar masses. Both panels of Figure 3 show an obvious dearth of companions with flux ratios $\Delta K \gtrsim 3$, corresponding roughly to the substellar mass range. Our survey should have clearly detected any source in this range of parameter space, as has been proven for orbital monitoring of field binaries like GJ 802 (Lloyd et al. 2006; Ireland et al. 2008), so this deficit seems to represent a genuine absence of companions.

Finally, we did not detect any candidate companions near the typical detection limits of our survey, which correspond to 99.9% confidence limits in any single separation bin or ∼99.5% across all separation bins. We would expect an average of 0.3 false detections for the 60 targets listed in Table 6, so our nondetection is consistent with the statistical estimate. We did detect four candidate companions with lower confidence levels (99.5%–99.9% in their separation bin, corresponding to overall confidence levels of ∼97.5%–99.5%). We would only expect to observe ∼1.5 false detections with this range of confidence levels, so four represents a marginally significant excess. A discussion of this is given in § 6.3.

5. THE STELLAR SEA

The properties of multiple star systems are important diagnostics for placing constraints on star formation processes. A comprehensive theory of star formation should be able to reproduce

TABLE 6

Upper Limits for Undetected Companions

Primary	Telescope	Δm[a]						q (m_s/m_p)[a]					
		10–20	20–40	40–80	80–160	160–240	240–320	10–20	20–40	40–80	80–160	160–240	240–320
GSC 06191−00552[b]	Palomar	...	3.12	4.71	5.03	4.97	...	...	0.110	0.028	0.025	0.034	...
GSC 06204−00812	Palomar	...	3.23	4.81	5.13	5.03	...	...	0.100	0.029	0.025	0.041	...
GSC 06205−00954	Palomar	...	2.46	4.02	4.50	4.42	...	...	0.157	0.042	0.035	0.050	...
GSC 06208−00834	Palomar	...	2.71	4.30	4.81	4.66	...	...	0.161	0.036	0.030	0.043	...
GSC 06209−01501	Palomar	...	2.62	4.19	4.53	4.49	...	...	0.166	0.039	0.032	0.034	...
GSC 06213−00194	Palomar	...	2.34	3.93	4.43	4.30	...	...	0.185	0.043	0.036	0.048	...
GSC 06213−00306	Palomar	...	2.32	3.89	4.13	4.10	...	...	0.089	0.051	0.041	0.047	...
GSC 06213−00306	Keck	3.23	5.06	5.89	5.80	5.54	5.20	0.098	0.020	0.014	0.015	0.026	0.019
GSC 06213−00306	Palomar	...	3.69	5.24	5.71	5.57	...	...	0.092	0.022	0.018	0.024	...
GSC 06213−01358	Palomar	...	2.66	4.25	4.70	4.58	...	...	0.143	0.038	0.032	0.052	...
GSC 06214−00210	Palomar	...	1.90	3.52	3.98	3.91	...	...	0.250	0.060	0.046	0.053	...
GSC 06214−02384	Palomar	...	2.88	4.45	4.86	4.76	...	...	0.182	0.043	0.028	0.044	...
GSC 06228−01359	Palomar	...	2.70	4.29	4.65	4.57	...	...	0.143	0.038	0.032	0.052	...
GSC 06793−00797	Keck	3.57	5.40	6.25	6.10	5.75	4.94	0.056	0.019	0.013	0.014	0.024	0.023
GSC 06793−00797	Palomar	...	2.14	3.71	4.21	4.10	...	...	0.222	0.062	0.038	0.047	...
GSC 06793−00806	Palomar	...	0.97	2.52	2.90	2.78	...	...	0.499	0.150	0.109	0.128	...
GSC 06793−00994	Palomar	...	3.65	5.23	5.49	5.40	...	...	0.153	0.032	0.024	0.036	...
GSC 06793−01406	Palomar	...	3.06	4.61	4.95	4.82	...	...	0.187	0.056	0.042	0.053	...
GSC 06794−00337	Palomar	...	2.70	4.29	4.60	4.51	...	...	0.190	0.047	0.034	0.039	...
GSC 06794−00480	Palomar	...	1.59	3.23	3.70	3.60	...	...	0.349	0.097	0.066	0.077	...
GSC 06794−00537	Palomar	...	3.31	4.87	5.18	5.08	...	...	0.100	0.026	0.023	0.031	...
RX J1551.1−2402	Keck	3.07	4.88	5.76	5.63	5.45	5.04	0.073	0.036	0.022	0.023	0.035	0.029
RX J1557.8−2305	Keck	2.98	4.81	5.78	5.55	5.13	3.96	0.084	0.028	0.018	0.020	0.033	0.039
RX J1558.2−2328	Keck	3.12	4.93	5.77	5.67	5.42	5.02	0.200	0.047	0.02	0.022	0.031	0.043
RX J1600.2−2417	Keck	2.72	4.55	5.27	5.18	4.80	4.26	0.109	0.029	0.022	0.023	0.030	0.034
RX J1600.6−2159	Palomar	...	2.93	4.52	4.95	4.86	...	...	0.177	0.043	0.027	0.042	...
RX J1600.7−2127	Palomar	...	2.44	4.05	4.47	4.38	...	...	0.187	0.043	0.034	0.040	...
RX J1601.1−2113	Palomar	...	2.64	4.23	4.68	4.62	...	...	0.143	0.039	0.032	0.053	...
RX J1602.0−2221	Keck	2.48	4.30	5.26	4.90	4.23	2.86	0.136	0.038	0.024	0.028	0.062	0.094
RX J1602.8−2401A	Keck	3.06	4.87	5.64	5.57	5.39	4.99	0.108	0.022	0.016	0.016	0.027	0.021
RX J1602.8−2401B	Palomar	...	2.52	4.08	4.58	4.50	...	...	0.167	0.042	0.031	0.035	...
RX J1603.6−2245	Palomar	...	3.10	4.65	4.94	4.90	...	...	0.143	0.037	0.027	0.029	...
RX J1603.9−2031A[b]	Palomar	...	2.86	4.45	4.94	4.86	...	...	0.143	0.033	0.027	0.039	...
RX J1604.3−2130	Keck	3.57	5.43	6.23	6.15	5.79	5.50	0.060	0.018	0.013	0.013	0.021	0.017
RX J1605.6−2152[b]	Keck	3.20	5.05	6.09	5.93	5.66	5.24	0.064	0.030	0.017	0.018	0.029	0.025
RX J1606.2−2036	Keck	2.99	4.83	5.72	5.54	5.05	4.05	0.094	0.025	0.017	0.018	0.022	0.034
RX J1607.0−2043	Keck	3.15	4.99	5.85	5.78	5.56	5.16	0.066	0.030	0.019	0.020	0.028	0.025
ScoPMS 021	Keck	3.37	5.19	6.06	5.94	5.75	5.05	0.081	0.020	0.013	0.014	0.016	0.020
ScoPMS 022	Keck	3.14	4.97	5.96	5.84	5.63	5.21	0.066	0.030	0.018	0.019	0.029	0.025
ScoPMS 028	Keck	3.02	4.85	5.64	5.54	5.40	4.86	0.078	0.031	0.021	0.022	0.027	0.029
ScoPMS 042b	Keck	3.22	5.07	5.85	5.72	5.48	4.99	0.075	0.034	0.025	0.026	0.040	0.034
ScoPMS 044	Palomar	...	2.48	4.05	4.38	4.29	...	...	0.182	0.05	0.035	0.053	...
ScoPMS 045[b]	Palomar	...	3.28	4.86	5.28	5.23	...	...	0.100	0.028	0.023	0.043	...
ScoPMS 048	Palomar	...	2.34	3.93	4.29	4.20	...	...	0.258	0.067	0.049	0.057	...
ScoPMS 060	Palomar	...	3.31	4.89	5.26	5.17	...	...	0.206	0.061	0.046	0.057	...
ScoPMS 214	Palomar	...	3.58	5.14	5.41	5.30	...	...	0.096	0.023	0.020	0.023	...
USco 155655.5−225839	Keck	3.48	5.31	6.23	6.15	5.95	5.60	0.050	0.025	0.015	0.015	0.018	0.020
USco 160142.6−222923	Keck	3.18	5.00	5.79	5.68	5.52	5.00	0.067	0.027	0.018	0.019	0.023	0.025
USco 160341.8−200557	Keck	3.66	5.50	6.39	6.28	5.88	5.38	0.053	0.028	0.017	0.017	0.027	0.026
USco 160343.3−201531	Keck	3.82	5.65	6.52	6.34	6.05	5.66	0.049	0.024	0.016	0.017	0.021	0.023
USco 160801.4−202741	Keck	3.31	5.13	6.06	6.00	5.71	5.32	0.057	0.026	0.016	0.016	0.024	0.022
USco 160822.4−193004	Keck	3.30	5.13	6.05	5.82	5.08	3.76	0.060	0.029	0.017	0.019	0.040	0.046
USco 160823.2−193001	Keck	3.79	5.64	6.46	6.35	6.20	5.77	0.041	0.019	0.013	0.014	0.016	0.017
USco 160825.1−201224	Keck	3.64	5.46	6.28	6.09	5.91	5.43	0.048	0.024	0.016	0.017	0.021	0.023
USco 160900.7−190852	Keck	3.81	5.63	6.38	6.33	6.14	5.72	0.040	0.019	0.013	0.014	0.015	0.018
USco 160916.8−183522	Keck	3.57	5.40	6.25	6.14	5.97	5.44	0.055	0.029	0.018	0.018	0.020	0.025
USco 160946.4−193735	Keck	3.59	5.42	6.28	6.18	5.98	5.56	0.049	0.024	0.016	0.016	0.022	0.022
USco 160954.4−190654	Keck	3.59	5.42	6.26	6.09	5.68	4.96	0.049	0.024	0.016	0.017	0.030	0.028
USco 161115.3−175721	Keck	3.80	5.63	6.45	6.31	6.15	5.72	0.045	0.024	0.015	0.016	0.023	0.020
USco 161347.5−183459	Keck	2.99	4.83	5.61	5.53	5.33	4.88	0.077	0.036	0.023	0.024	0.055	0.032
USco 161358.1−184828	Keck	3.72	5.56	6.45	6.38	6.19	5.80	0.051	0.024	0.016	0.017	0.018	0.021
V1149 Sco	Palomar	...	3.49	5.06	5.43	5.35	...	...	0.154	0.038	0.025	0.035	...

[a] The range of each separation bin is reported in units of mas, and the corresponding detection limits are reported in terms of δm or q.

[b] We detected candidate companions at lower confidence (97.5%–99.5%) for these four sources; we plan to obtain additional observations to confirm or disprove them.

TABLE 7
Companions Identified with Direct Imaging

Name	Telescope	Δm (mag)	Separation (mas)	P.A. (deg)
New				
GSC 06191−00019	Palomar	0.85 ± 0.01	845.8 ± 1	58.0 ± 0.1
GSC 06195−00768	Palomar	0.54 ± 0.01	558 ± 1	292.1 ± 0.3
RX J1550.9−2534	Keck	0.03 ± 0.01	127.5 ± 1	72.70 ± 0.06
RX J1558.1−2405[a]	Palomar	1.86 ± 0.03	197 ± 2	98.8 ± 0.3
RX J1607.0−2036	Palomar	0.15 ± 0.03	183.8 ± 1	344.2 ± 0.3
ScoPMS 015	Palomar	0.58 ± 0.02	124.1 ± 1	166.5 ± 0.4
ScoPMS 017[a]	Keck	0.65 ± 0.01	57.1 ± 1	68.34 ± 0.11
USco 160428.4−190441	Keck	0.04 ± 0.01	881.1 ± 1	128.13 ± 0.10
USco 160707.7−192715[a]	Keck	1.59 ± 0.01	91.8 ± 1	2.1 ± 0.3
USco 160823.8−193551	Keck	0.98 ± 0.01	651.5 ± 1	64.61 ± 0.11
Known				
GSC 06204−01067	Palomar	2.10 ± 0.01	2528 ± 4	93.04 ± 0.02
GSC 06213−00306	Palomar	2.37 ± 0.01	3186 ± 5	305.11 ± 0.01
GSC 06793−00806	Palomar	1.19 ± 0.01	1907 ± 3	338.81 ± 0.03
GSC 06793−00868	Palomar	0.37 ± 0.01	1981 ± 4	155.29 ± 0.06
RX J1602.8−2401B	Palomar	2.91 ± 0.02	7198 ± 13	352.22 ± 0.04
ScoPMS 048	Palomar	1.76 ± 0.01	3394 ± 5	191.22 ± 0.01
ScoPMS 042b	Keck	2.48 ± 0.03	4606 ± 2	6.71 ± 0.03
USco 160908.4−200928	Keck	0.32 ± 0.01	2042 ± 1	139.36 ± 0.07
USco 161031.9−191305	Palomar	3.83 ± 0.02	5775 ± 9	112.66 ± 0.02

[a] Uncertainties are difficult to estimate due to significant blending of the PSFs. The values and uncertainties from the aperture masking detection in Table 5 should be used for this system.

the observed separation distribution, mass ratio distribution, and total fraction of binary systems, as well as any mass or environmental dependencies of these properties. The mass ratio distribution also plays a critical role in defining the brown dwarf desert since the bottom tail of the distribution represents the upper bound of the desert.

Most recent efforts to model binary formation have typically assumed that stellar and prestellar interactions play a key role in establishing binary properties. The most popular type of model assumes that a cluster of 5–10 protostellar embryos forms from a single turbulently fragmenting cloud core (e.g., Kroupa 1995; Sterzik & Durisen 1998; Kroupa & Bouvier 2003; Kroupa et al. 2003; Delgado-Donate et al. 2003; Hubber & Whitworth 2005); these embryos would then undergo mass accretion and dynamical evolution to form single stars and stable multiple systems. However, other stellar properties place strong limits on the rate of early dynamical evolution. Close stellar encounters would tend to dissipate or truncate disks, with smaller stars having fewer and shorter lived disks, but there is no evidence for this trend (e.g., White & Basri 2003; Luhman 2004; Scholz et al. 2006). Dynamical encounters might also eject lower mass stars and brown dwarfs, but no such ejected population is seen (Luhman 2006), although some models suggest that strong ejections might be rare (Bate & Bonnell 2005). Finally, any dynamically active environment would truncate the stellar binary separation distribution for all stars in the association. The absence of low-mass wide binaries has often been interpreted as a sign of this process, but this absence is seen even in environments where the wide binary frequency is very high for solar-mass stars (Kraus & Hillenbrand 2007a), so it may have another explanation.

Modeling efforts that concentrate on other binary formation processes have not advanced sufficiently to make any rigorous prediction. These processes, which are summarized by Goodwin & Kroupa (2007), include fragmentation of massive circumstellar disks, the role of magnetic support in prestellar cores, and fission of quasi-static rotating cores. All of these processes are more significant for isolated cores than for the dynamically active turbulent fragmentation scenario discussed above, so the limits on dynamical activity of young stars suggest that they should be considered in more detail in the future.

Given the absence of theoretical predictions, we are left only with empirical comparisons to other samples. Previous field multiplicity surveys (DM91; Fischer & Marcy 1992, hereafter FM92; Reid & Gizis 1997, hereafter RG97) have suggested a range of possible results for the separation distribution, mass ratio distribution, and total frequency of binary systems. We compare our results to these surveys and to the expected result if binary companions are drawn from an IMF. None of these explanations produce an acceptable fit for our mass ratio distribution, so the next step is to test other analytic distributions. Our number statistics do not support strong constraints on this analysis yet, so we limit our analysis to a single functional form (the lognormal distribution) until we conclude the second half of our survey, an examination of young stars in Taurus.

Finally, we note that two of the systems among our sample (USco 160428.4−190441 and USco 160825.1−201224) would have fallen below the optical flux limit of our sample ($R \leq 14$, imposed by the AO system) if the primaries were single. Including these systems in our statistical analysis would bias our results toward higher binary frequencies, so we have omitted them from our subsequent analysis. There is also an opposing effect due to the inclusion of unresolved binary pairs (which we identify as single stars) that would be omitted by the same criterion if we knew they were binaries. We obviously cannot identify these systems, so we only note that the effect should be small. If the binary frequency at small separations is ∼10%–20% and the mass ratio

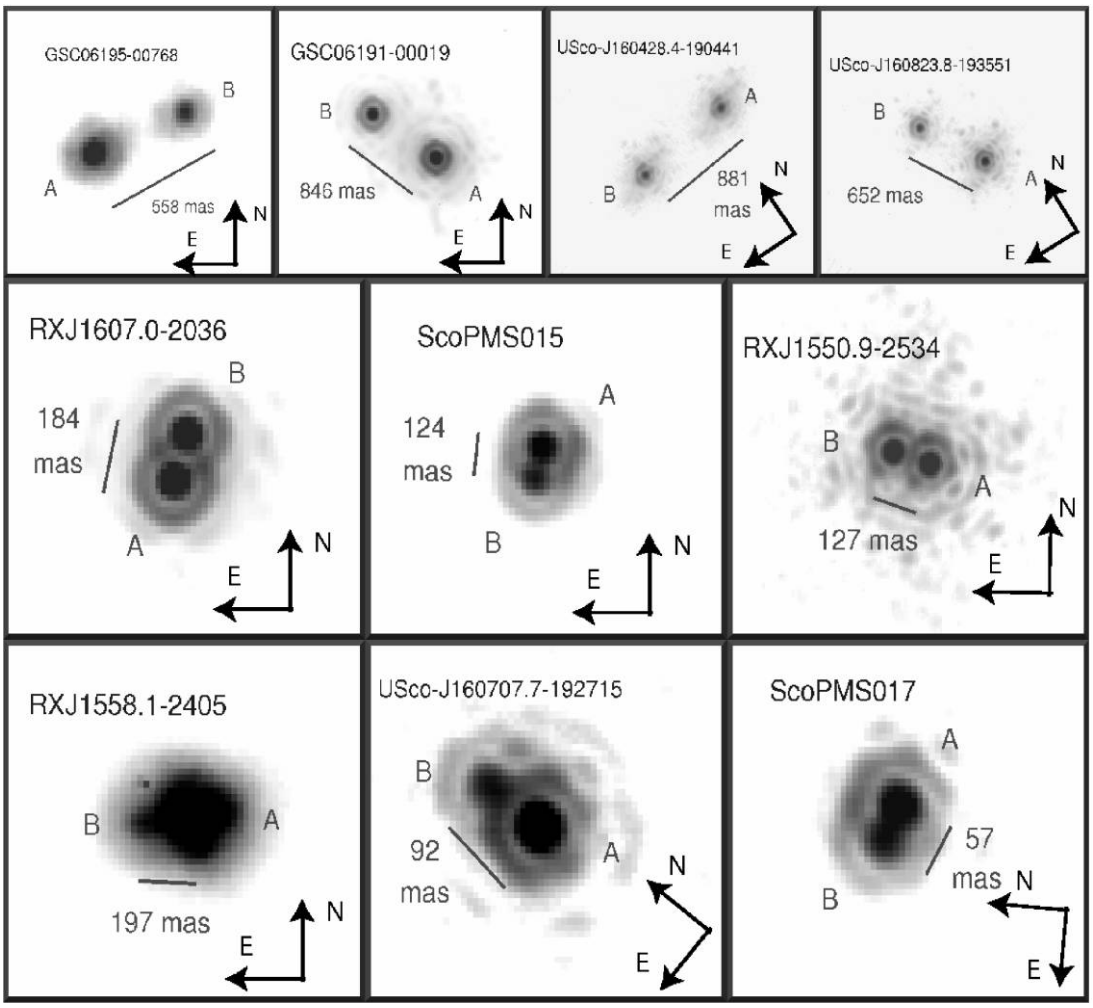

FIG. 3.—Ten new systems that we observed with direct imaging. The top row shows relatively wide (0.5″–1.0″) pairs; the middle row shows close, equal-flux pairs that are still easily distinguished; and the bottom row shows three very close or unequal-flux systems that could be difficult to identify with direct imaging alone but were easily identified with aperture masking. [*See the electronic edition of the Journal for a color version of this figure.*]

distribution is similar to the distribution we observe, then no more than one to two unresolved systems should be included as "single stars." This systematic bias should not be significant compared to the statistical uncertainties in our results. We also note that our entire analysis must implicitly adopt the assumption that the mass ratio distribution and separation distribution are uncorrelated over the survey's separation range. This assumption has not been rigorously tested, but a simultaneous investigation of both parameters would require a far larger sample.

5.1. *The Mass Ratio Distribution*

Observations of field stars have suggested that the mass ratio distribution is strongly dependent on mass. DM91 showed that F and G stars have mass ratio distributions biased toward inequal masses, roughly consistent with a truncated Gaussian distribution (albeit with few constraints for $q < 0.1$). By contrast, FM92 and RG97 found a distribution for early M dwarfs that is roughly flat, and numerous surveys have shown that the distribution for late M dwarfs and brown dwarfs is biased toward equal masses ($q \gtrsim 0.7$; Close et al. 2003; Bouy et al. 2003; Burgasser et al. 2003). However, these surveys have all studied old field populations. Simulations show that dynamical evolution is typically not significant once a star enters the field (e.g., Weinberg et al. 1987), but a large fraction of stars are thought to be drawn from dense cluster environments (like the Orion Nebula Cluster or the Pleiades), so their properties could have been shaped by significant dynamical evolution in their natal environment. This suggests that primordial binary properties could differ significantly from those of their older brethren.

In the left panels of Figure 6, we plot histograms of the mass ratio distribution for our entire sample of 99 stars, only the higher mass stars (46 FGK dwarfs, representing masses $\gtrsim 0.7\ M_{\odot}$), and only the lower mass stars (55 M dwarfs, representing masses $\lesssim 0.7\ M_{\odot}$). The mass ratio distributions are plotted for projected separations of 0.04″–3.0″ (6–435 AU), where the inner bound is defined by the inner limit for our survey to be sensitive to $q \sim 0.04$ and the outer bound is defined by the field star contamination rate predicted for Upper Sco binaries by Kraus & Hillenbrand (2007a). All of the number statistics are only moderately significant, but they still suffice for placing limits on the range of functional forms for the primordial mass ratio distribution.

In all three cases, our survey's mass ratio distribution is not strongly inconsistent with a constant distribution, so our ability to test more complex functional forms is limited. However, our data will suffice to test previously suggested functions. To this end, we have compared our results to three distributions: a Gaussian distribution like that suggested by DM91, a constant distribution like that suggested by FM92, and a distribution that was

TABLE 8
Companion Properties

Name	Separation	q (m_s/m_p)	$M_{\rm prim}$ ($M_\odot$)	$M_{\rm sec}$ ($M_\odot$)	Source
GSC 06191−00019	122.6	0.50	0.82	0.41	Palomar-Imaging
GSC 06195−00768	80.9	0.65	0.77	0.50	Palomar-Imaging
GSC 06204−01067	366.6	0.19	0.49	0.09	Palomar-Imaging
GSC 06209−00735	3.6	0.18	1.12	0.21	Palomar-Masking
GSC 06213−00306	462.0	0.15	0.87	0.13	Palomar-Imaging
GSC 06214−00210	318.6	0.02	0.60	0.011	Palomar-Imaging
GSC 06764−01305	7.9	0.10	0.99	0.10	Keck-Masking
GSC 06780−01061	217.5	0.35	0.36	0.13	Kraus & Hillenbrand (2007a)
GSC 06793−00569	207.4	0.14	1.25	0.18	Metchev (2005)
GSC 06793−00806	276.5	0.40	0.60	0.24	Palomar-Imaging
GSC 06793−00819	32.2	0.91	1.35	1.23	Metchev (2005)
GSC 06793−00868	287.3	0.73	0.60	0.44	Palomar-Imaging
GSC 06794−00156	6.4	0.90	1.59	1.43	Keck-Masking
RX J1550.0−2312	3.9	0.56	0.49	0.28	Keck-Masking (1)
RX J1550.0−2312	3.9	0.56	0.49	0.28	Keck-Masking (2)
RX J1550.9−2534	18.5	1.00	1.75	1.74	Keck-Imaging
RX J1558.1−2405	33.0	0.17	0.95	0.16	Palomar-Masking
RX J1558.1−2405	28.6	0.25	0.95	0.23	Palomar-Imaging
RX J1600.5−2027	27.4	0.69	0.60	0.41	Köhler et al. (2000)
RX J1601.7−2049	29.7	0.60	0.68	0.41	Köhler et al. (2000)
RX J1601.8−2445	11.0	0.45	0.77	0.35	Köhler et al. (2000)
RX J1601.9−2008	5.7	0.36	1.62	0.58	Palomar-Masking
RX J1602.8−2401B	1043.7	0.10	0.95	0.10	Palomar-Imaging
RX J1602.9−2022	45.0	0.90	0.77	0.69	Köhler et al. (2000)
RX J1603.9−2031B	17.6	0.63	0.68	0.43	Köhler et al. (2000)
RX J1606.6−2108	185.5	0.91	0.60	0.55	Köhler et al. (2000)
RX J1607.0−1911	86.9	0.31	0.60	0.19	Köhler et al. (2000)
RX J1607.0−2036	26.7	0.87	0.68	0.59	Palomar-Imaging
ScoPMS 005	111.1	0.48	1.66	0.80	Köhler et al. (2000)
ScoPMS 013	13.3	0.62	0.54	0.34	Köhler et al. (2000)
ScoPMS 015	18.0	0.60	0.68	0.41	Palomar-Imaging
ScoPMS 016	192.0	0.60	0.64	0.38	Köhler et al. (2000)
ScoPMS 017	7.8	0.54	0.60	0.32	Keck-Masking
ScoPMS 017	8.3	0.59	0.60	0.35	Keck-Imaging
ScoPMS 019	3.7	0.97	0.60	0.58	Keck-Masking
ScoPMS 020	28.0	0.64	0.36	0.23	Köhler et al. (2000)
ScoPMS 023	43.5	0.61	0.87	0.53	Köhler et al. (2000)
ScoPMS 027	6.3	0.66	1.12	0.74	Palomar-Masking
ScoPMS 029	93.2	0.65	0.49	0.32	Köhler et al. (2000)
ScoPMS 031	83.8	0.59	0.64	0.38	Köhler et al. (2000)
ScoPMS 042a	43.4	0.70	0.60	0.42	Köhler et al. (2000)
ScoPMS 048	492.1	0.30	1.35	0.40	Palomar-Imaging
ScoPMS 052	20.9	0.53	1.35	0.71	Metchev (2005)
USco 160428.4−190441	127.8	0.97	0.36	0.35	Keck-Imaging
USco 160517.9−202420	2.3	0.75	0.36	0.27	Keck-Masking
USco 160707.7−192715	15.3	0.16	0.49	0.08	Keck-Masking
USco 160707.7−192715	13.3	0.28	0.49	0.14	Keck-Imaging
USco 160823.8−193551	94.5	0.46	0.60	0.28	Keck-Imaging
USco 160908.4−200928	296.1	0.77	0.24	0.18	Keck-Imaging
USco 161031.9−191305	21.1	0.09	0.77	0.07	Keck-Masking
USco 161031.9−191305	837.4	0.04	0.77	0.03	Palomar-Imaging

Notes.—Typical uncertainties in separations are ∼15% and result from the unknown depth of each system within the association. The uncertainties in masses are dominated by systematic errors, including a global zero-point uncertainty of ∼20% and individual uncertainties of as much as ∼100% due to the possibility of further unresolved multiplicity. The mass ratio estimates should be more precise (∼5%–10%) since many systematics (distance, age, extinction, and zero-point shifts) are canceled, but they are still vulnerable to large systematic errors due to unresolved multiplicity.

assembled by assuming that stars are randomly drawn from the IMF of Upper Sco. None of these functions feature a low-mass cutoff that could explain the brown dwarf desert, so we have also conducted preliminary tests of a new functional form: the lognormal distribution. Our constraints on this distribution are not very stringent, but they allow some preliminary conclusions. We summarize the results for each of these tests in the following subsections, and we report the goodness-of-fit statistics (as measured with χ^2 and Kolmogorov-Smirnov tests) in Table 9. The Kolmogorov-Smirnov test is more sensitive in cases where the bin size is a

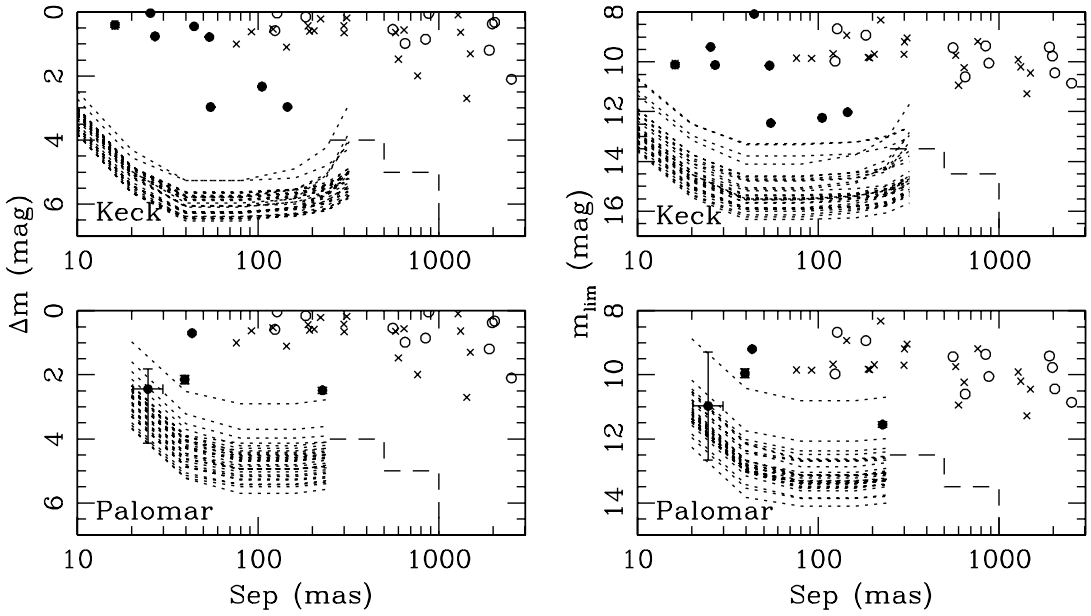

FIG. 4.—Contrast ratio (*left*) and secondary brightness (*right*) as a function of separation for our new systems identified via masking (*filled circles*) and imaging (*open circles*), plus all known binary systems (*crosses*). We also show the corresponding aperture masking detection limits for all apparently single stars in our survey (*short-dashed lines*) and our adopted sensitivity limits for our imaging data (*long-dashed line*).

significant fraction of the total range of parameter space or when the trial distribution function changes rapidly across a bin, so all of our conclusions are based on its results.

5.1.1. *The Gaussian Distribution*

DM91 found that the mass ratio distribution for field F and G dwarfs could be well fitted by a Gaussian distribution centered at low q-values ($\mu = 0.23$, $\sigma = 0.42$). Their survey was not sensitive to substellar companions ($q < 0.1$), but if this functional form is valid, it suggests that substellar companions should be very common ($f \sim 10\%$, with 4% falling in our survey's separation range). However, there are no physical motivations for assuming that an arbitrarily chosen segment of a Gaussian function (-0.5 to $+2.0\,\sigma$) should predict the mass ratio distribution, so any similarity may be a coincidence. In the left panels of Figure 6, we plot the q distribution suggested by DM91 with a dotted line. This distribution was originally defined for all separations, but DM91 found that only 40% of their systems fell within our survey's separation range, so we have scaled their function by this amount. This ensures that the overall binary frequency and the shape of the distribution are directly comparable.

Visual inspection shows that our full sample's q distribution is more biased toward equal-mass companions than that of DM91, an observation that is supported by goodness-of-fit tests. This level of disagreement could be a result of our wider mass range than DM91's sample since lower mass binary systems are thought to have mass ratios that are not as biased toward low masses. The relative levels of agreement for our high-mass and low-mass

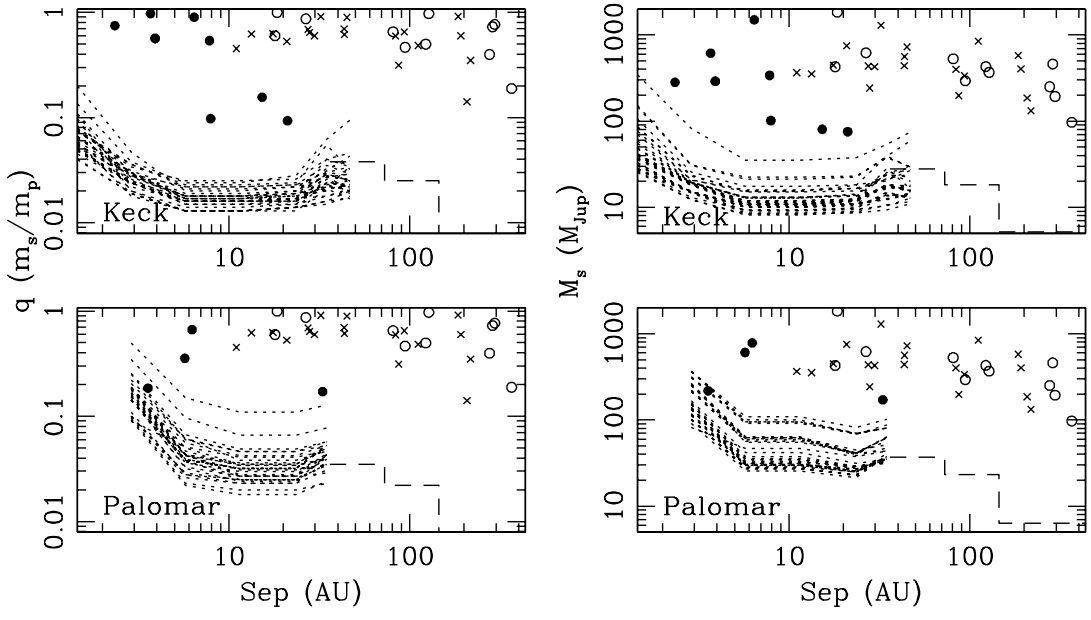

FIG. 5.—Same as Fig. 4, but showing mass ratio (*left*) and secondary mass (*right*) as a function of separation.

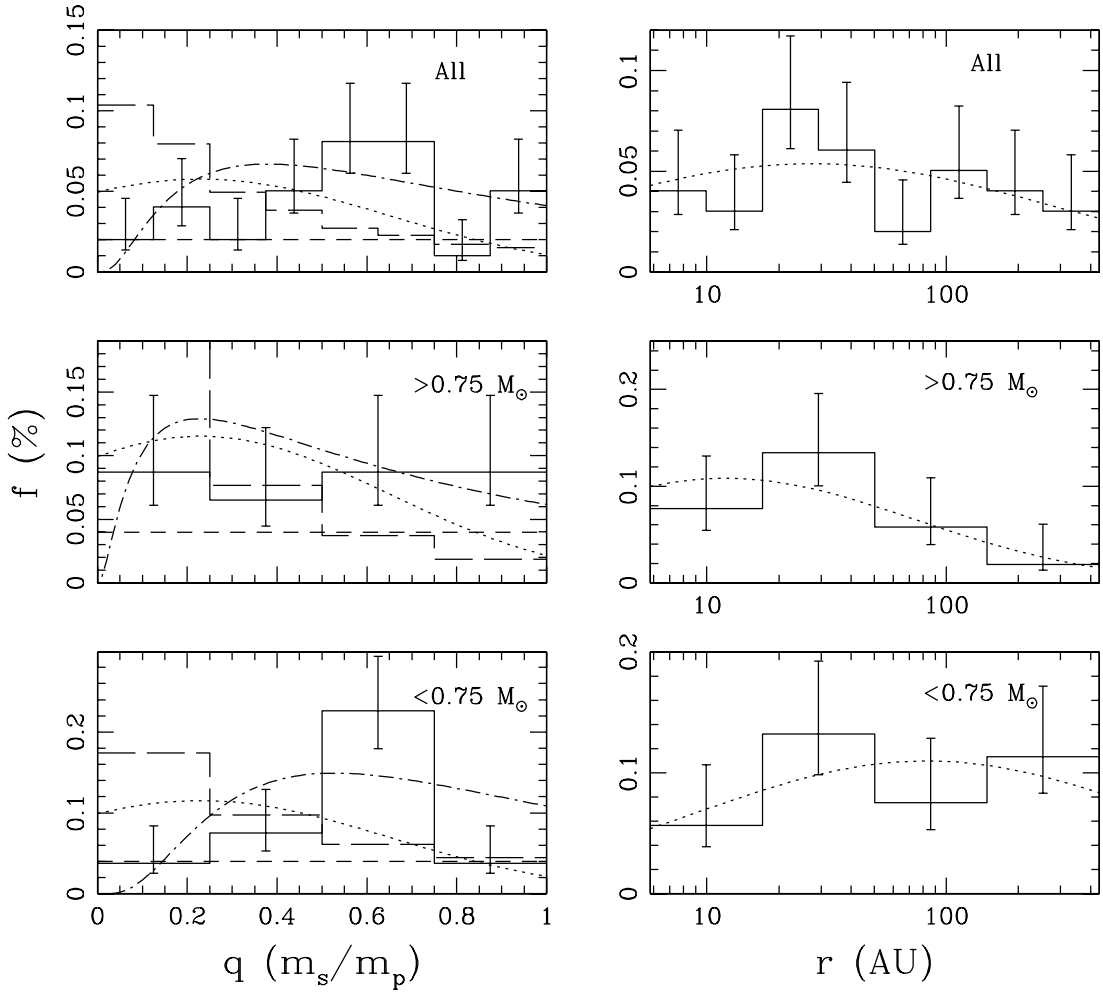

FIG. 6.—Mass ratio distributions (*left*) and separation distributions (*right*) for all stars in our sample (*top*), the more massive half (FGK stars; $M > 0.75\ M_{\odot}$; *middle*), and the less massive half (M stars; $M < 0.75\ M_{\odot}$; *bottom*). On the left, we overplot several suggested mass functions: a truncated Gaussian distribution (*dotted line*), a constant distribution (*short-dashed line*), a distribution of companions drawn from the IMF (*long-dashed line*), and the best-fit lognormal distribution (*dot-dashed line*). On the right, we overplot the best-fit lognormal distribution (*dotted line*) for each subsample. [*See the electronic edition of the Journal for a color version of this figure*.]

TABLE 9
BINARY MASS RATIO DISTRIBUTIONS

Distribution	Masses	χ^2	P	$D_{\rm K\text{-}S}$	P
Gaussian	All	21.2	0.007	0.35	0.00025
	High	5.1	0.28	0.34	0.047
	Low	13.6	0.009	0.41	0.0016
Constant (16%)	All	31.9	0.0001	...	...
	High	11.5	0.021	...	...
	Low	18.3	0.0011	...	...
Constant (35%)	All	11.4	0.18	0.19	0.14
	High	0.17	0.997	0.18	0.67
	Low	11.1	0.025	0.24	0.17
IMF	All	37.0	0.000005	0.46	0.0000004
	High	14.0	0.003	0.52	0.0003
	Low	21.3	0.00009	0.44	0.0005
Lognormal	All	9.7	0.14	0.15	0.41
	High	1.5	0.47	0.21	0.49
	Low	7.6	0.022	0.22	0.23

subsamples support this assessment; the high-mass subsample is only somewhat inconsistent with the DM91 distribution, while the low-mass subsample is very significantly inconsistent.

5.1.2. *The Constant Distribution*

A field binary survey by FM92 found that the mass ratio distribution for field early M dwarfs seemed to be better fitted by a flat distribution of mass ratios for $q \gtrsim 0.4$. RG97 found that this flat distribution extends to much lower mass ratio distributions for M dwarfs, although they also suggested the existence of a possible peak near unity ($q \gtrsim 0.8$). As with the Gaussian distribution, a flat distribution would suggest that substellar companions are not uncommon relative to stars, but these survey were not sensitive enough to actually detect most brown dwarf secondaries. Their total binary fractions (20^{+7}_{-5} % for $q > 0.4$ or 16^{+7}_{-4} % for all q, respectively, in this separation range) are marginally inconsistent, but the RG97 sample (which is more rigorously volume limited) contains 17 of the 37 binary systems considered by FM92, so we adopt their value. In the three left panels of Figure 6, we plot the flat q distribution suggested by RG97 with a short-dashed line.

Visual inspection suggests that a constant distribution might be more appropriate for our sample's q distribution than the DM91 Gaussian distribution. However, the flat distribution of RG97

appears to fall systematically too low for the full sample and both subsamples, yielding high χ^2 values. If we renormalize the flat distribution to match our overall binary frequency (36^{+5}_{-4}%), we find much better agreement. The corresponding Kolmogorov-Smirnov tests, which only measure the cumulative density function and implicitly include our renormalization, also find that a constant distribution is consistent or perhaps marginally inconsistent. We also note that we found no clear evidence of an excess of equal-mass binaries; the 2 σ upper limit in the highest mass bin of our entire sample ($q > 0.875$) is $f < 11.4\%$.

5.1.3. *A Distribution Drawn from the IMF*

Some theories also suggest that binary companions could be drawn randomly from the IMF. This idea used to be popular since it could be naturally explained as a result of random pairing and because previous results were moderately consistent, but it has fallen out of favor as the role of dynamical interactions has been increasingly constrained. However, an IMF could still be valid for wide binaries (which may form during the turbulent fragmentation of a large cloud core), and it is not clear where this regime ends and where the binary fragmentation of a collapsing protostar begins. This suggests that it would be prudent to test the validity of an IMF-based q distribution. We adopted our IMF (hereafter the companion mass function, or CMF) from the spectroscopic membership surveys of Preibisch et al. (1998, 2002), Slesnick et al. (2006a), and Slesnick (2007); this IMF can be described by a broken power law, $\Psi(M) = dN/dM \propto M^{-\alpha}$, where $\alpha = -2.8$ for $0.6\ M_\odot < M < 2.0\ M_\odot$, $\alpha = -0.9$ for $0.15\ M_\odot < M < 0.6\ M_\odot$, and $\alpha = -0.6$ for $0.02\ M_\odot < M < 0.15\ M_\odot$.

We derived the expected q distribution for our sample by assuming that every binary primary had a companion randomly drawn from the lower mass regime of the CMF. Most implementations of this process use Monte Carlo simulations to draw a suitable population from the CMF, but our CMF is defined as a simple analytic function, so we chose to directly convert it into a q distribution: $dN/dq = (dN/dM_{\rm sec})(dM_{\rm sec}/dq) \propto \Psi(qM_{\rm prim})/M_{\rm prim}$, where the full distribution $f(q)$ is the normalized sum of all functions dN/dq as defined for each binary primary. In the left panels of Figure 6, we plot our IMF-based q distribution with a long-dashed line. Unlike the previous two distributions, our IMF-based distribution is fundamentally different for our entire sample and for each subsample since they represent different sets of primary masses.

The bottom-heavy nature of the IMF suggests that of all sources with masses $\lesssim 1\ M_\odot$, approximately $\frac{1}{4}$ should be substellar and many of the rest should fall at the very bottom of the stellar mass range. This distribution disagrees very significantly with our results, and all statistical tests conclusively rule out the possibility that the companions in our sample might have been randomly drawn from the IMF.

5.1.4. *A Parameterized Lognormal Distribution*

As well as simply testing fixed distributions, we can use Bayesian analysis to draw conclusions about the most likely models from a class of distributions. We chose distributions that are lognormal in q (base-10), with a mean at $q = 1$. We chose this distribution because it is based on the following ad hoc model: beginning with two equal-mass cores, we accrete matter stochastically onto the two cores such that the mean accretion rate onto each core is proportional to the core mass. Applying the central limit theorem to the logarithm of the core mass ratio, we arrive at a lognormal distribution in q. This distribution also has the important property that the functional form is the same in $1/q$ as in q, meaning that it does not matter whether the "primary" or "secondary" star is used as the reference for calculating q. Among differentiable q distributions, only distributions that have an asymptotic power-law slope of -1 at $q = 1$ can be written so that they have this property. This distribution has a corresponding probability density function

$$f(q) = \frac{\exp(-\log q^2/2\sigma^2)}{q}. \quad (1)$$

The likelihood function is then given by

$$L(\{q_i\}|\sigma) = \Pi_i \frac{\exp\left(-\log q_i^2/2\sigma^2\right)/q_i}{\int_{0.04}^{1.0} \exp(-\log x^2/2\sigma^2)/x\,dx}. \quad (2)$$

The normalization in this equation explicitly includes our lower limit for q. Using a uniform prior on σ, we find that the best-fit value of σ is $0.428^{+0.059}_{-0.049}$. This is our best-fit distribution of all tested distributions and predicts that only 1.2% of all companions are brown dwarfs in our separation range (meaning $q < 0.08$ here). It reproduces the peak in the companion distribution at $q \sim 0.4$ similar to that seen by DM91, but without the lack of near equal-mass companions predicted by their preferred distribution.

The low-mass subsample has a best-fit value of σ of $0.347^{+0.063}_{-0.049}$, and the high-mass subsample has a best-fit σ of $0.528^{+0.148}_{-0.092}$. These values of σ are significantly different at the 96% level. This demonstrates that the lower mass subsample prefers more equal-mass companions to the higher mass subsample, consistent with results for low-mass binaries in the field. We have plotted all three best-fitting lognormal distributions in the right panels of Figure 6 (*dot-dashed line*).

5.2. *The Binary Separation Distribution*

Field surveys have also suggested that the separation distribution depends strongly on mass; the shape seems to be lognormal for a wide range of masses, but the mean and maximum separations decline with decreasing mass. DM91 found that the separation distribution for solar-mass stars has a mean separation of $\sim$30 AU and some binaries as wide as 10^4 AU. FM92 and RG97 found that early M binaries have a mean separation that is marginally consistent (4–30 AU), but few have separations $\gtrsim 10^3$ AU. Finally, recent surveys have shown that late M dwarfs and brown dwarfs have very small mean and maximum separations (4 and 20 AU, respectively; Close et al. 2003; Bouy et al. 2003; Burgasser et al. 2003). As we described above, many field stars formed in denser environments, so there has probably been some dynamical evolution that disrupted wide binaries. However, surveys of older clusters (e.g., Patience et al. 2002) suggest that the old binary population is only severely depleted by intracluster dynamical interactions at separations of $\gtrsim$100–200 AU. This suggests that only the outer edge of our sample's separation distribution should differ significantly from the field.

Interpretation of the companion separation distribution is usually complicated by observational realities. The most meaningful quantity to consider is the distribution of semimajor axes, but the semimajor axis can only be determined as part of an orbital solution. Some authors convert the projected separation for each star into an estimated semimajor axis using a single corrective factor (typically $a = 1.26r$), but this choice is only valid on a statistical level and carries implicit assumptions about the eccentricity distribution that are extrapolated from much shorter period binaries. Therefore, we choose to report the observed projected separation distribution only. In the right panels of Figure 6, we plot histograms of the separation distributions for our entire sample,

only the higher mass FGK stars, and only the lower mass M dwarfs. This distribution spans separations of 6–435 AU, the range where our survey is sensitive to most brown dwarf companions.

We find that the separation distribution for our sample is consistent with a distribution constant with $\log r$, with r the apparent separation on the sky. A one-sided Kolmogorov-Smirnov test over the separation range 6–435 AU gives $D = 0.13$, with $p = 0.57$. In order to examine what our separation distribution is not consistent with, we have also attempted to fit lognormal distributions over the separation range 6–435 AU, where the likelihood of a particular value of the mean μ and standard deviation σ is given by

$$L(\{r_i\}|\mu, \sigma) = \Pi_i \frac{\exp\left[-(\mu - \log r_i)^2/2\sigma^2\right]}{\int_{\log r_{\min}}^{\log r_{\max}} \exp\left[-(\mu - x)^2/2\sigma^2\right] dx}. \quad (3)$$

As in the previous subsection, the normalization on the denominator is an explicit integral rather than the standard normalization for a Gaussian because of our artificial truncation of the distribution at 6 and 435 AU. We take the prior distribution of μ to be uniform between 0 and 3 (i.e., median separations between 1 and 1000 AU), and the prior distribution of σ to be uniform between 0 and 2. The most likely values of μ and σ are then 1.44 and 1.01 for the entire sample, 1.08 and 0.79 for the high-mass sample, and 1.92 and 0.97 for the low-mass sample. However, integrating over all μ, the most likely value of σ is our upper limit of 2, demonstrating that the data are consistent with an approximately flat distribution. The most important point to come out of this analysis is that the 90% confidence lower limit on σ is 0.94, suggesting that we have detected at most two-thirds of the companions in our sample, with the remaining companions being at smaller or greater separations.

The separation distributions for the high- and low-mass samples follow the opposite trend to that suggested in the literature. Our low-mass sample has a median separation of 81 AU, while our high-mass sample has a median separation of 21 AU. This difference is not statistically significant since both distributions are consistent with a constant distribution, and a two-sided Kolmogorov-Smirnov test gives a difference statistic $D = 0.30$, with $p = 0.36$. It is interesting, however, that we do not see the trend toward smaller separations with lower masses as seen in field dwarfs (e.g., Allen [2007], who finds $\mu = 0.86$ and $\sigma = 0.28$ for ultracool field dwarfs). We hope to repeat this analysis with more conclusive results after we complete our survey sample.

5.3. *The Total Binary Fraction*

The total binary fraction, representing the integrated separation and mass ratio distributions, provides a useful comparison for different populations. It does not provide any additional information about the binary formation process that is not implicitly included in its component distributions, but it is very useful in other contexts like correcting the IMF for undetected multiplicity or relating the IMF to the prestellar core mass function. Previous surveys suggest that the binary fraction is close to unity for early-type stars, declining to ~60% for solar-mass stars and ~30% for early M stars; in all cases, ~40%–50% of binaries fall within the same separation range as our survey (6–435 AU).

We found binary fractions of 35^{+5}_{-4} % for our entire sample, 33^{+7}_{-5} % for our high-mass (FGK) subsample, and 38^{+7}_{-6} % for our low-mass (early M) subsample. The first two results are roughly consistent with those observed in the field, but the second result is significantly higher than the value observed in the field. A survey of wide multiplicity has found that there are only four binaries with separations of 3″–30″ among our sample members (Kraus & Hillenbrand 2007a; A. Kraus & L. Hillenbrand 2008, in preparation), but there are likely to be a significant number at smaller separations; we discovered some of these binaries inside the nominal completeness limit of our survey, and future RV surveys are likely to uncover many more. If the binary fraction at separations $\lesssim$6 AU is as high in Upper Sco as in the field, then the binary fraction for early M dwarfs in Upper Sco could be as high as is observed for field F–G dwarfs ($\gtrsim$60%).

6. THE FARTHEST SHORE?

In the past 15 years, the search for extrasolar planets has become one of the major goals of the astronomical community. RV searches have discovered hundreds of planets and allowed us to probe the dynamics of planetary systems (e.g., Marcy et al. 2005), and more recently, transit searches have uncovered dozens of additional planets and allowed us to study their fundamental properties (masses and radii; O'Donovan et al. 2007; Torres 2007). However, the direct observation of extrasolar planetary systems has proven to be an elusive goal. Advances in high-resolution imaging (mostly aimed at speckle suppression) are allowing for increasingly strict upper limits on their existence, but no planetary companions at separations comparable to our own solar system have been directly imaged yet. An intriguing sample of candidate planetary-mass companions have been identified at much wider separations (e.g., Chauvin et al. 2004; Neuhäuser et al. 2005), but their mass and formation mechanism are still uncertain.

The difficulty of directly detecting extrasolar planets with existing methods suggests that a change of strategy is in order. Previous surveys have typically used spectral or rotational differential imaging (Masciadri et al. 2005; Biller et al. 2007; Lafreniere et al. 2007) to cancel AO speckles, although some surveys have also used direct imaging (typically in the mid-infrared; Kasper et al. 2007) and simply accepted the inherent limits from speckle noise. All of these surveys produce their deepest limits at wide separations ($\gtrsim$0.5″), so they can only probe the regime of likely planet formation (5–30 AU) for relatively nearby stars ($d \lesssim 30$ pc); even for these stars, existing surveys cannot probe deep enough to identify old ($\tau \gtrsim 1$ Gyr) planets, so they must study intermediate-age ($\tau \sim 10$–200 Myr) members of nearby moving groups. By contrast, our survey achieves its deepest limits at much smaller angular separations, so we can probe deeper into the planetary separation regime of nearby moving group members (M. J. Ireland & A. L. Kraus 2008, in preparation) and finally systematically survey the nearest very young associations like Upper Sco.

However, we must include a cautionary note: the fact that we found no high-confidence planetary detections could allow us to place upper limits on the existence of massive Jupiter analogs, but as we have previously described, it could also show that current models severely overestimate the luminosity of young planets. The core accretion models that predicted this underluminosity have difficulty producing 10 $M_{\rm Jup}$ planets, so it is possible that massive planets are formed via disk fragmentation (which may not suffer this underluminosity). However, all of our subsequent results should be taken with some skepticism. We list all of our detection limits in Table 6, so if the models are updated in the future, it should be trivial to reanalyze our results and produce new limits.

6.1. *Modeling the Population of Young Planets*

We expect that the planetary population over our range of interest will be described by three parameters: the total frequency f, a power-law mass distribution $dN/dM \propto M^{\alpha}$, and a power-law

semimajor axis distribution $dN/da \propto a^{\beta}$. We can place constraints on these parameters by simulating a population of planetary systems for each set of parameters and then convolving this population with our detection limits to determine the level of consistency with our nondetection. Our survey's detection limits cannot be directly translated into limits on the planetary population since planets could be obscured by projection effects, so for each simulated planet, we also invoke a random inclination angle, a random true anomaly, and an eccentricity drawn from the approximately Gaussian distribution observed for RV planets (Juric & Tremaine 2007). We note that Juric & Tremaine (2007) chose to fit their eccentricity distribution with a Schwarzschild function, but given the uncertainties in the observational statistics, it is not possible to determine whether a Schwarzschild or Gaussian function is more appropriate. We have adopted the more computationally convenient form.

Our specific implementation uses a mass drawn from between 1 and 30 $M_{\rm Jup}$, a semimajor axis drawn from between 3 and 36 AU, and an eccentricity drawn from a Gaussian distribution between 0.0 and 0.8 with mean $\mu_e = 0.3$ and standard deviation $\sigma_e = 0.3$. We do not directly model the planetary frequency f in our Monte Carlo routine because it can be added analytically. We adopted the upper mass limit (30 $M_{\rm Jup}$) to match the most massive T Tauri disks at ages of 1–2 Myr (only $\sim$1% of which significantly exceed this mass; Andrews & Williams 2005). After conducting our simulations for a range of values of f, α, and β, we compiled a three-dimensional probability density function $P(f, \alpha, \beta)$ that corresponds to the probability that we would have detected a planet and then extracted three-dimensional confidence surfaces that correspond to the 50%, 90%, 95%, and 99% probabilities that our observations actually would have found no planets.

6.2. *Limits on the Population of Young Planets*

It is difficult to present a set of three-dimensional confidence surfaces in a two-dimensional medium, so we have chosen to present a selection of two-dimensional slices where we fix one parameter to its current best-estimated value. The statistics of RV surveys have finally become significant enough to suggest possible values of our distribution parameters, so we have adopted these canonical values ($f = 5\%$, $\alpha = -1.05$, $\beta = -1.0$; Marcy et al. 2005) to produce our three confidence plots. The canonical distribution values are derived from RV surveys; they have found the power-law exponents α and β for their sample of (short-period) planets, and they extrapolate that $\sim$5% of their sample members have long-term linear RV trends suggestive of massive long-period planets. The power-law exponents may not be valid since many gas giants at small separations are thought to have migrated there, but these values represent the best constraint available.

In the three panels of Figure 7 we present the joint confidence intervals for each pair of values if we fix the third value to the canonical estimate. These results suggest that the canonical planetary distribution can only be ruled out at the $\sim$50% level. This is not a statistically significant level, but it is much better than any previous imaging survey could have achieved. We also find that a much higher planetary frequency is significantly ruled out for most values of α and β; the only values that are consistent require either the mass function or the separation distribution to be very steep, placing most planets in a regime that our survey cannot search. Otherwise, we cannot rule out significant regions of parameter space. In particular, if the canonical planetary frequency ($f = 5\%$) is accurate, then we cannot place any constraints beyond the 70% level on values of α or β. This is a straightforward result of our sample size; with 60 targets, a frequency of 5% suggests that only three wide planets exist in our sample. Only unrealistically top-heavy mass or separation distributions would place a significant number of planets in our survey's detection limits.

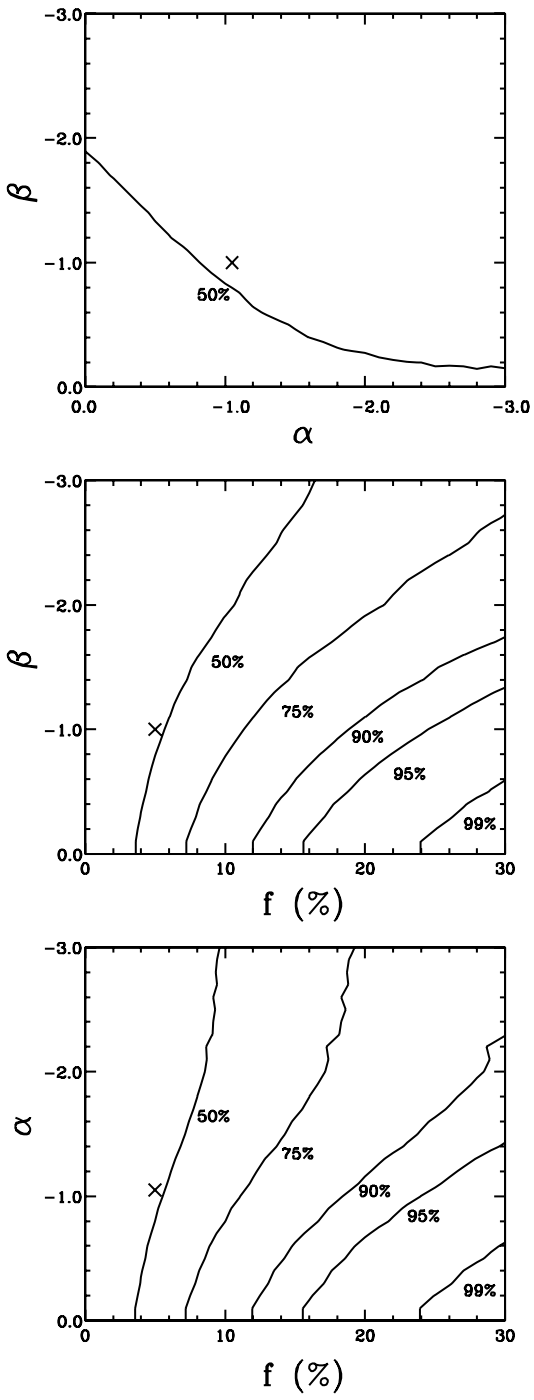

FIG. 7.—Our survey's joint limits on the total giant planet frequency f, the mass function power law α, and the semimajor axis distribution power law β, assuming that we fix each parameter at the canonical value suggested by RV surveys (e.g., Marcy et al. 2005): $f = 5\%$ (*top*), $\alpha = -1.05$ (*middle*), and $\beta = -1.0$ (*bottom*). In each case, we also denote the confidence level corresponding to all three canonical values with crosses. [*See the electronic edition of the Journal for a color version of this figure.*]

Finally, we can determine a direct constraint on the total frequency of wide high-mass planets by adopting the canonical values for both α and β, reducing the confidence surface to a confidence interval. If we assume that $\alpha = -1.05$ and $\beta = -1.0$, then there is a 90% probability that $f < 19\%$ and a 95% probability that

$f < 24\%$. We cannot place similar limits on α and β because these confidence limits correspond to a total of 2.3 and 3.0 expected detections, respectively; if the total planetary frequency is only $f = 5\%$, then only extremely top-heavy power laws would allow for that many expected detections among our 60 targets.

6.3. *An Ocean in the Distance?*

Our survey did not identify any faint companions at a confidence level of $\gtrsim$99.5%, but it did identify four faint candidate companions at confidence levels of 97.5%–99.5%. Based on our total sample size (60 targets), the expected number of spurious detections with a confidence level >97.5% is only $\sim$1.5; according to Poisson statistics, the probability of identifying four or more of these spurious detections is only 7%, so this seems to represent a marginally significant excess. We will try to obtain follow-up observations for each marginal detection in the upcoming observing season; given their faintness, any genuine companion in this group could represent the first directly imaged massive Jupiter analog.

7. HOW ARID IS THE BROWN DWARF DESERT?

Many multiplicity surveys suggest that the binary companion mass function declines as it enters the brown dwarf mass range, and all results from RV surveys suggest the same for the planetary mass function. In light of these results, it is not surprising that brown dwarf companions are uncommon. The interesting question is whether they are more uncommon than predicted by the tails of both mass functions; if so, then this deficit genuinely represents a brown dwarf "desert."

Our results suggest that the stellar mass ratio distribution is constant or at least not biased heavily toward low-mass companions. Given our observed total binary fraction (35^{+5}_{-4} %), a constant mass ratio distribution predicts that $\sim$3.5% of all stars should have a substellar or nearly substellar companion with $q \leq 0.1$ at separations of 6–435 AU. We have found two such companions ($1.8^{+2.3}_{-0.6}$ %), a result that is entirely consistent with that claim. However, both companions fall at the upper end of this range ($q = 0.10$ and 0.09), and only one is possibly substellar ($M_{\rm sec} \sim 0.07\ M_{\odot}$); given the uncertainties inherent to our estimates of stellar properties, it is not inconceivable that both companions could fall in the range $q > 0.1$. This would be consistent with estimates for wide companions to much higher mass Upper Sco members; Kouwenhoven et al. (2007) found that only $0.5\% \pm 0.5\%$ of the B and A stars in Upper Sco have substellar companions with separations of 130–520 AU.

Our estimate of the contribution from planetary formation processes is much more uncertain. If the planetary distribution is truly defined by the canonical values given in the literature ($f = 5\%$, $\alpha = -1.05$, and $\beta = -1.0$) and the models describing luminosities of young planets are correct, then our survey would have had a 50% chance of detecting one "planetary" companion of any mass $<30\ M_{\rm Jup}$. This probability would have been higher if the planetary mass function extended beyond $30\ M_{\rm Jup}$ with no cutoff, but even a cutoff at $100\ M_{\rm Jup}$ would imply that our null detection is significant at only $\sim$75%. As a result, we cannot state with any confidence that the canonical values are incorrect or that there is any sort of high-mass cutoff in the planetary mass function.

8. SUMMARY

We present the results of a survey for stellar and substellar companions to 82 young stars in the nearby OB association Upper Scorpius. This survey used nonredundant aperture mask interferometry to achieve typical contrast limits of $\Delta K \sim 5$–6 at the diffraction limit, revealing 12 new companions that lay below the detection limits of traditional high-resolution imaging; we also summarize a complementary snapshot imaging survey that discovered seven directly resolved companions. The overall frequency of binary companions ($\sim 33^{+5}_{-4}$ % at separations of 6–435 AU, including companions reported in the literature) appears to be similar to field stars of similar mass, but the companion mass function appears to be more biased toward equal-mass companions than the equivalent mass function in the field. This result could indicate an environmental or dynamical effect, but our number statistics are not yet sufficient to place strong constraints on its nature.

Our survey limits encompass the entire brown dwarf mass range and we detected two companions with $q \leq 0.1$, a number that is consistent with a flat mass ratio distribution. However, both of these companions have mass ratios near 0.1 and only one has a mass that might fall below the substellar boundary, so we hesitate to rule out the existence of any deficit that might denote a brown dwarf desert. Our survey's deep detection limits also extend into the top of the planetary mass function; we have not identified any planetary companions at high confidence ($\gtrsim$99.5%), but we have identified four candidate companions at lower confidence ($\gtrsim$97.5%) that merit additional follow-up to confirm or disprove their existence. The lack of planets within the brown dwarf mass range also is not a significant proof of the existence of a desert.

Finally, we note that our survey results are extremely encouraging with respect to the potential for future discoveries. We are currently extending our survey efforts to the Taurus-Auriga star-forming region and to several nearby moving groups, and this expansion of our sample should make any conclusions much more robust. Our ability to precisely measure astrometry for close ($\sim$2–3 AU) binary systems could also allow us to measure dynamical masses for many young stars on a timescale of $\lesssim$5 yr. Finally, achieving similar detection limits for planetary-mass companions in Taurus-Auriga and the nearby moving groups will significantly enhance our limits on the properties of young planets; a similar null detection for our full sample would significantly rule out the canonical values for the planetary distribution function, confirming either that these values are wrong or that evolutionary models significantly overestimate the luminosity (and detectability) of young planets.

The authors thank Lynne Hillenbrand for helpful feedback on the manuscript and Brian Cameron for sharing his NIRC2 astrometric calibration results prior to publication. We also thank the referee, Ralph Neuhäuser, for providing a helpful critique. We recognize and acknowledge the very significant cultural role and reverence that the summit of Mauna Kea has always had within the indigenous Hawaiian community. We are most fortunate to have the opportunity to conduct observations from this mountain.

A. L. K. is supported by a NASA/Origins grant to Lynne Hillenbrand. M. I. would like to acknowledge Michelson Fellowship support from the Michelson Science Center and the NASA Navigator Program. This work is also partially supported by the National Science Foundation under grants 0506588 and 0705085. This work makes use of data products from the Two Micron All Sky Survey, which is a joint project of the University of Massachusetts and IPAC/Caltech, funded by NASA and the NSF. Our research has also made use of the USNOFS Image and Catalogue Archive operated by the United States Naval Observatory, Flagstaff Station (http://www.nofs.navy.mil/data/fchpix/).

APPENDIX

THE DETECTION LIMITS OF NONREDUNDANT APERTURE MASK OBSERVATIONS

For each set of n frames (called a "run"), with $n \geq 8$, we calculate the mean closure phase vector $\bar{\phi}$ and an estimate for the covariance matrix of closure phase:

$$\hat{C}_r = \frac{\Sigma_i \left(\phi_i - \bar{\phi}\right)^t \left(\phi_i - \bar{\phi}\right)}{n-1}. \tag{A1}$$

Here ϕ_i is the closure phase vector calculated for a single frame and superscript t represents a transpose. The variance in closure phase calculated by this technique (the diagonal of $\hat{C}_r$) will be called $\hat{\sigma}_r^2$.

Studentizing all statistics was seen as an excessively difficult task, given the high number of dimensions in our data set, the strong correlations between measured parameters, and the need to have fast, automatic fitting routines. In order to limit susceptibility to the lack of a tail in the Gaussian approximation for uncertainties that follow a Student's t distribution, we artificially increased the errors on closure phases with the smallest errors. We did this by applying an error cutoff at $\frac{2}{3}$ of the median closure phase error. In the case of closure phases with equal true errors, this means that we would have artificially increased the uncertainties on 12% of the closure triangles, changing the expected value of reduced χ^2 from 1.4 to 1.24 for $n = 8$, making a smaller difference for large n.

In addition to the error calculated from a single run, we calculated closure phase uncertainties from the dispersion among calibrator observations. We denote these variances $\hat{\sigma}_c^2$. Where the error calculated from dispersion among the calibrators was greater than that given by the standard error of the mean for a single run, we weighted the error estimates by

$$\hat{\sigma}^2 = \frac{2\hat{\sigma}_r^2 + (n_c - 1)\hat{\sigma}_c^2}{n_c + 1}. \tag{A2}$$

After errors were increased by either the scatter among calibrators or the closure phase uncertainty histogram cutoff, the covariance matrix was modified in such a way that the correlation matrix remained unchanged.

After finding the covariance matrix of calibrated closure phase, we found that in general the errors in its calculation caused excessive noise in calculation of the covariance matrix inverse. For this reason, we first filtered the covariance matrix by fitting a model of the form

$$\mathrm{Var}\left(\theta_{ijk}\right) = \frac{\sigma_f^2}{\left\langle \left| V_i V_j V_k \right| \right\rangle} + \mathrm{Var}(\theta_i) + \mathrm{Var}\left(\theta_j\right) + \mathrm{Var}(\theta_k) \tag{A3}$$

and

$$\mathrm{Cov}\left(\theta_{ijk}, \theta_{jlm}\right) = \pm \mathrm{Var}(\theta_i). \tag{A4}$$

$\mathrm{Var}(\theta_i)$ is a model variance of phase for baseline i, which in turn has the form

$$\mathrm{Var}(\theta_i) = \sigma_i^2 + \alpha\left(m_{tx} m_{tx}^t + m_{ty} m_{ty}^t\right). \tag{A5}$$

Here σ_i is the intrinsic phase variance of baseline i, α is a free parameter, and m_{tx} and m_{ty} are closure phase modes caused by skewness of the image in x- and y-directions. This skewness is caused by temporal effects, where in a single exposure, tip/tilt errors can be asymmetrical, with, e.g., a single "glitch" where for 10% of the exposure the image is offset by 20 mas. This can be a dominant error term at Palomar, where the tip/tilt mirror is too large to have an adequate correction bandwidth in poor seeing. The $\pm$ in equation (A4) is a plus sign if baseline i is counted in the same direction for both closure phases and a minus sign if baseline i is counted in opposite directions for both closure phases.

Finally, in the fitting process, reduced χ^2 was often greater than 1. Although by chance this should have occurred 50% of the time if uncertainties were correctly estimated, in practice it occurred $\sim$90% of the time. A possible reason for this could be residual systematics differences in sky position or color, despite the care taken to minimize these differences in a single observing block. When this occurred, additional systematic closure phase uncertainties were added so that reduced χ^2 was 1. For determining the confidence level of a null detection, this reduced χ^2 corresponds to the reduced χ^2 for a single star fit, and for determining errors on a nonnull detection, this reduced χ^2 corresponds to that for the best binary fit.

Due to the linear dependence of model closure phases, we calculate χ^2 on a closure phase vector space with dimensionality equal to the number of independent closure phases, N_{ind}. This vector space V_{ind} is formed by projection via a matrix T_p, defined so that the covariance matrix on V_{ind} is a diagonal matrix D:

$$D = T_p C^{-1} T_p^t. \tag{A6}$$

This means that, given a closure phase vector $\phi_{\boldsymbol{d}}$, the covariance matrix of the linear combination $T_p\phi_{\boldsymbol{d}}$ is given by the diagonal matrix D. Given model closure phases $\phi_{\boldsymbol{m}}$ and data $\phi_{\boldsymbol{d}}$, the value of χ^2 is then given by

$$\chi^2 = (\phi_{\boldsymbol{m}} - \phi_{\boldsymbol{d}})^t T_p^t D T_p (\phi_{\boldsymbol{m}} - \phi_{\boldsymbol{d}}). \tag{A7}$$

It is this χ^2 that was minimized when fitting binary functions to closure phase. The Monte Carlo procedure was simplified computationally by limiting the fitting procedure to the high-contrast regime, where closure phase is a linear function of companion brightness. In this regime, model closure phases $\phi_{\boldsymbol{m}}$ were found for each separation and position angle for a fixed contrast ratio R_m, with the fitted contrast ratio given by

$$R = R_m \frac{\sigma \mathbf{Z}^t D T_p \phi_{\boldsymbol{m}}}{\phi_{\boldsymbol{m}}^t T_p^t D T_p \phi_{\boldsymbol{m}}}. \tag{A8}$$

The matrix $\sigma\mathbf{Z}$ is a standard normal vector of length $N_{\rm ind}$, multiplied by the standard errors as calculated in the vector space $V_{\rm ind}$. This equation is relatively simple to derive by minimizing χ^2 where the model closure phase at contrast R is $(R/R_m)\phi_{\boldsymbol{m}}$.

REFERENCES

Ahmic, M., Jayawardhana, R., Brandeker, A., Scholz, A., van Kerkwijk, M., Delgado-Donate, E., & Froebrich, D. 2007, ApJ, 671, 2074
Allen, P. 2007, ApJ, 668, 492
Andrews, S., & Williams, J. 2005, ApJ, 631, 1134
Ardila, D., et al. 2000, AJ, 120, 479
Baraffe, I., Chabrier, G., Allard, F., & Hauschildt, P. 1998, A&A, 337, 403
Baraffe, I., Chabrier, G., Barman, T., Allard, F., & Hauschildt, P. 2003, A&A, 402, 701
Bate, M., & Bonnell, I. 2005, MNRAS, 356, 1201
Bessell, M., & Brett, J. 1988, PASP, 100, 1134
Biller, B., et al. 2007, ApJS, 173, 143
Bouy, H., et al. 2003, AJ, 126, 1526
———. 2006, A&A, 451, 177
Brandner, W., et al. 1996, A&A, 307, 121
Burgasser, A., et al. 2003, AJ, 125, 850
Cameron, P. B. 2008, Ph.D. thesis, Caltech
Chabrier, G., et al. 2000, ApJ, 542, 464
Chauvin, G., Lagrange, A., Dumas, C., Zuckerman, B., Mouillet, D., Song, I., Beuzit, J., & Lowrance, P. 2004, A&A, 425, L29
Chiu, K., Fan, X., Leggett, S. K., Golimowski, D. A., Zheng, W., Geballe, T. R., Schneider, D. P., & Brinkmann, J. 2006, AJ, 131, 2722
Close, L., et al. 2003, ApJ, 587, 407
Delgado-Donate, E., Clarke, C. J., & Bate, M. R. 2003, MNRAS, 342, 926
de Zeeuw, P., Hoogerwerf, R., de Bruijne, J., Brown, A., & Blaauw, A. 1999, AJ, 117, 354
Duquennoy, A., & Mayor, M. 1991, A&A, 248, 485 (DM91)
Fischer, D., & Marcy, G. 1992, ApJ, 396, 178 (FM92)
Gizis, J., Kirkpatrick, J. D., Burgasser, A., Reid, I. N., Monet, D., Liebert, J., & Wilson, J. 2001, ApJ, 551, L163
Goodwin, S., & Kroupa, P. 2007, in Protostars and Planets V, ed. B. Reipurth, D. Jewitt, & K. Keil (Tucson: Univ. Arizona Press), 133
Grether, D., & Lineweaver, C. 2006, ApJ, 640, 1051
Guenther, E., Esposito, M., Mundt, R., Covino, E., Alcalá, J., Cusano, F., & Stecklum, B. 2007, A&A, 467, 1147
Hillenbrand, L., & White, R. 2004, ApJ, 604, 741
Houk, N., & Smith-Moore, M. 1988, Michigan Spectral Survey (Ann Arbor: Dept. Astron. Univ. Mich.)
Hubber, D., & Whitworth, A. 2005, A&A, 437, 113
Ireland, M., et al. 2008, ApJ, submitted
Johnson, J., et al. 2006, ApJ, 647, 600
Juric, M., & Tremaine, S. 2007, ApJ, submitted (astro-ph/0703160)
Kasper, M., Apai, D., Janson, M., & Brandner, W. 2007, A&A, 472, 321
Kirkpatrick, J. D., et al. 2000, AJ, 120, 447
Köhler, R., et al. 2000, A&A, 356, 541
Kouwenhoven, M. B. N., Brown, A. G. A., & Kaper, L. 2007, A&A, 464, 581
Kraus, A., & Hillenbrand, L. 2007a, ApJ, 662, 413
———. 2007b, ApJ, 664, 1167
Kraus, A., White, R., & Hillenbrand, L. 2006, ApJ, 649, 306
Kroupa, P. 1995, MNRAS, 277, 1491
Kroupa, P., & Bouvier, J. 2003, MNRAS, 346, 369
Kroupa, P., et al. 2003, MNRAS, 346, 354
Kunkel, M. 1999, Ph.D. thesis, Max-Planck-Institut für Astronomie
Lafreniere, D., et al. 2007, ApJ, 670, 1367
Leggett, S., Allard, F., & Hauschildt, P. 1998, ApJ, 509, 836
Lissauer, J., & Stevenson, D. 2007, in Protostars and Planets V, ed. B. Reipurth, D. Jewitt, & K. Keil (Tucson: Univ. Arizona Press), 591
Lloyd, J., Martinache, F., Ireland, M., Monnier, J., Pravdo, S., Shaklan, S., & Tuthill, P. 2006, ApJ, 650, L131
Lohmann, A. W., Weigelt, G., & Wirnitzer, B. 1983, Appl. Opt., 22, 4028
Luhman, K. 2004, ApJ, 602, 816
———. 2006, ApJ, 645, 676
Luhman, K., et al. 2003, ApJ, 593, 1093
Marcy, G., & Butler, R. 2000, PASP, 112, 137
Marcy, G., Butler, R., Fischer, D., Vogt, S., Wright, J., Tinney, C., & Jones, H. 2005, Prog. Theor. Phys. Suppl., 158, 24
Marley, M., Fortney, J., Hubickyj, O., Bodenheimer, P., & Lissauer, J. 2007, ApJ, 655, 541
Martin, E., et al. 2004, AJ, 127, 449
Martinache, F., Lloyd, J., Ireland, M., Yamada, R., & Tuthill, P. 2007, ApJ, 661, 496
Masciadri, E., Mundt, R., Henning, Th., Alvarez, C., & Barrado y Navascues, D. 2005, ApJ, 625, 1004
McCarthy, C., & Zuckerman, B. 2004, AJ, 127, 2871
Metchev, S. 2005, Ph.D. thesis, Caltech
Naef, D., et al. 2007, A&A, 470, 721
Nakajima, T., et al. 1989, AJ, 97, 1510
Neuhäuser, R., & Guenther, E. 2004, A&A, 420, 647
Neuhäuser, R., Guenther, E., Alves, J., Huélamo, N., Ott, Th., & Eckart, A. 2003, Astron. Nachr., 324, 535
Neuhäuser, R., Guenther, E., Wuchterl, G., Mugrauer, M., Bedalov, A., & Hauschildt, P. 2005, A&A, 435, L13
O'Donovan, F., et al. 2007, ApJ, 663, L37
Patience, J., et al. 2002, AJ, 123, 1570
Pravdo, S., et al. 2006, ApJ, 649, 389
Preibisch, T., Brown, A., Bridges, T., Guenther, E., & Zinnecker, H. 2002, AJ, 124, 404
Preibisch, T., Guenther, E., & Zinnecker, H. 2001, AJ, 121, 1040
Preibisch, T., et al. 1998, A&A, 333, 619
Reid, I., & Gizis, J. 1997, AJ, 113, 2246 (RG97)
Schmidt-Kaler, Th. 1982, Physical Parameters of the Stars, Landolt-Bornstein Numerical Data and Functional Relationships in Science and Technology, Vol. 2b (Berlin: Springer)
Scholz, A., Jayawardhana, R., & Wood, K. 2006, ApJ, 645, 1498
Skrutskie, M., et al. 2006, AJ, 131, 1163
Slesnick, C. 2007, Ph.D. thesis, Caltech
Slesnick, C., Carpenter, J., & Hillenbrand, L. 2006a, AJ, 131, 3016
Slesnick, C., Carpenter, J., Hillenbrand, L., & Mamajek, E. 2006b, AJ, 132, 2665
Stephenson, C. B. 1986, ApJ, 300, 779
Sterzik, M., & Durisen, R. 1998, A&A, 339, 95
Stetson, P. 1987, PASP, 99, 191
Torres, G. 2007, ApJ, 671, L65
Tuthill, P., et al. 2000, PASP, 112, 555
Walter, F., et al. 1994, AJ, 107, 692
Weinberg, M., Shapiro, S., & Wasserman, I. 1987, ApJ, 312, 367
White, R., & Basri, G. 2003, ApJ, 582, 1109
Whitworth, A., & Stamatellos, D. 2006, A&A, 458, 817
Zacharias, N., Urban, S., Zacharias, M., Wycoff, G., Hall, D., Monet, D., & Rafferty, T. 2004, AJ, 127, 3043